PHYSICAL REVIEW FLUIDS **10**, 093603 (2025)

Weakly deformable poroelastic particle in an unbounded Stokes flow

Simon M. Finney,[1,*] Matthew G. Hennessy,[2] Andreas Münch,[1] and Sarah L. Waters[1,†]
[1] *Mathematical Institute, University of Oxford, Oxford OX2 6GG, United Kingdom*
[2] *School of Engineering Mathematics and Technology, University of Bristol, Bristol BS8 1TW, United Kingdom*

(Received 6 September 2024; accepted 21 July 2025; published 23 September 2025)

A framework is developed to study the deformation of a spherical poroelastic particle immersed in an unbounded, three-dimensional Stokes flow. The flow is driven by imposing a steady far-field condition, and the particle is modeled using a two-phase approach, where a deformable solid skeleton is fully saturated by the surrounding viscous fluid. Slip is permitted on the interface between the poroelastic particle and the surrounding Stokes flow. We consider the regime in which the ratio of typical viscous fluid stress to elastic stiffness is small, leading to small deformations and a decoupling of the fluid and solid problems. The traction exerted by the fluid on the particle and the Darcy pressure within are computed and used to formulate a purely solid-mechanics problem for the equilibrium particle deformation. To demonstrate the method, two example far-field flow profiles (shear flow and Poiseuille flow) are considered. Closed-form solutions for the translational velocity, rotation, and surface deformation of the particle are presented and analyzed as functions of the particle's permeability, slip, and Poisson's ratio. We show that the rotation of the particle is not impacted by its poroelasticity and that the Poisson's ratio plays a key role in selecting the dominant mechanism of particle deformation. For incompressible particles, the shear traction exerted by the fluid on the particle drives the deformation, causing the deformation to decrease with slip. For compressible particles, the Darcy pressure in the particle drives the deformation, and the deformation increases with slip.

DOI: 10.1103/p3g6-gkww

I. INTRODUCTION

Understanding the mechanical response of a poroelastic particle suspended in an external fluid flow is central to a wide range of biomedical and engineering applications. For example, hydrogel particles, which may be modeled as poroelastic when in chemical equilibrium, may be injected into the body to deliver drug payloads to a specific site [1–3]. However, the pressure-driven flow during injection can generate large shear stresses that damage the hydrogels and cause the premature release of drug molecules. Similarly, in flow cytometry and other microfluidic assays, soft biological cells are exposed to controlled flows such as shear or Poiseuille profiles, and their resulting deformation is used to infer material properties such as the Young's modulus [4–6]. Understanding the relationships between the particle's permeability, elasticity, and surface slip on the resulting translational and rotational velocity and the particle deformation is therefore desirable and would enable similar empirical measurements for poroelastic particles.

---

[*] Contact author: finney@maths.ox.ac.uk
[†] Contact author: sarah.waters@maths.ox.ac.uk

Beyond material characterization, mechanical forces play an essential role in understanding cell behavior. Fluid-induced surface stresses can trigger mechanotransduction pathways, where mechanical stimuli lead to changes in gene expression through membrane stretching or cytoskeletal signaling [7–11]. The ability to accurately predict surface stresses and deformation is therefore foundational for interpreting cellular responses to flow. Modeling poroelastic bodies in viscous fluids is particularly relevant to newly developed cell therapies, where hydrogel-coated donor cells are injected into the body [12,13]. These encapsulations can be modeled as a poroelastic core-shell structure, and mathematical analyses can produce new insights into how stress from the external viscous fluid propagates into the cell via the poroelastic coating.

The mechanical response of a poroelastic particle arises from the interplay between the external fluid flow, its elasticity and interstitial fluid flow, coupling conditions at the interface between the surrounding fluid and the particle, and the confinement of the external flow by boundaries. It remains unclear how these interactions combine to control the stress and deformation experienced by a poroelastic particle, along with its translational and rotational velocity. The aim of this paper is, therefore, to develop a theoretical model that provides mechanistic insights into how a poroelastic particle responds to an arbitrary external unbounded Stokes flow. We provide analytical solutions for the flow and poroelastic stress within the system, and the resulting translational and rotational velocities of the particle as well as its deformation. We illustrate how this solution can be applied to a particle in a tube, in the limit that the particle is small compared to the tube radius. These mechanistic insights can be deployed to tune material properties and driving forces of the system to achieve the target particle response. Alternatively, these insights will enable the properties of soft porous materials to be inferred from experimental measurements of particle shape and translation/rotational motion.

Typically, poroelastic structures are modeled using a biphasic approach, where an elastic solid skeleton is coupled to an interstitial viscous fluid through conservation of mass and momentum [14,15]. Whittaker [16] used volume averaging to show that the macroscopic flow through a rigid porous medium with a small pore size is governed by Darcy's law, in which the fluid flow is given by the product of the permeability and the pressure gradient. If the fluid volume fraction is large ($>95\%$) an additional viscous term is added to Darcy's law, leading to Brinkman flow [17]. In this work we consider only Darcy's law, though we note that extension to Brinkman flow is possible [18].

Much work has been done to understand the motion of a neutrally buoyant, rigid porous sphere suspended in a Stokes flow. Yang and Hong [19] obtained analytic expressions for the flow in a single spherical Brinkman particle exposed to linear unbounded flows such as axisymmetric straining flow and linear shear flow. This work was later extended to consider the impact of an external planar interface on the particle's motion [20,21]. More recent theoretical studies have considered the effect of other external boundaries on particle mobility through a viscous fluid, with examples including pressure-driven flow through a cylindrical tube or an external spherical cavity [22–24].

The theoretical study of poroelastic particles in a surrounding viscous flow has received less attention than their rigid counterpart. Consequently, studies of poroelastic particles in a viscous flow are predominantly numerical, often utilizing techniques such as the immersed boundary method [25] and the arbitrary Lagrangian-Eularian (ALE) method to accurately capture the dynamics of the fluid-structure interaction [26–29].

Small-deformation asymptotic reductions of fluid-structure interaction problems are not uncommon and greatly simplify the couplings between the fluid and solid mechanics [4,30–32]. Specifically, by assuming the ratio of typical viscous stress in the exterior flow to the solid skeleton's elastic stiffness is small, the deformation of the particle will be small. Hence, the particle can be treated as linearly poroelastic and the interfacial conditions can be imposed on the undeformed boundary. Under this assumption, the fluid flow, particle velocity, and particle rotation decouple from the particle deformation. The fluid flow is determined by prescribing the background flow with no particle (this is given by the far-field flow) and adding a local correction to satisfy the interfacial conditions on the particle surface. Once calculated, the surface tractions and internal Darcy pressure are then computed and used to calculate the resulting particle deformation. Villone *et al.* [33] and Finney *et al.* [34] validated this asymptotic approach when applied to a stiff, incompressible, elastic particle under tube flow, showing strong agreement with finite element solutions especially when the elastic particle is small. Obtaining analytical solutions is desirable for inferring parameter values from experiments. For example, Mietke *et al.* [35] calculated the elastic stiffness of a single cell translating through a microfluidic tube, modeling the cell as a stiff elastic particle.

Young *et al.* [32] used the small deformation asymptotic reduction to calculate the equilibrium shape of a weakly deformable poroelastic particle under a linear flow, where the fluid velocity depends linearly on the spatial coordinates. In this work, we provide a framework to analytically calculate the small deformation of a poroelastic particle when exposed to any unbounded Stokes flow, such that the fluid velocity may depend nonlinearly on the spatial coordinates, allowing more complex external flows to be analyzed. The framework is a direct extension of the work of Murata [30] who considered an incompressible and impermeable elastic particle in any unbounded flow. To demonstrate the power of the framework, we present two example far-field flow profiles, shear flow and Poiseuille flow. The former case was also considered by Young *et al.* [32], though we do not provide quantitative comparison since different interfacial conditions were imposed. The latter case, which is relevant to many biological applications such as drug delivery systems, cannot be investigated using the approach of Young *et al.* [32] and has not previously been presented.

When the external flow involves an external boundary, for example, Poiseuille flow, adding a local correction to the background flow disrupts the no-flow boundary conditions on the external tube wall. However, this disruption is small if the particle is far from the boundary [30]. Maintaining the assumption of small deformation, semianalytic methods, such as the method of reflections developed by Brenner and Happel [36], can be used to capture the effect of an external boundary more accurately. Finney *et al.* [34] employed these methods, along with numerical simulations, for the case of an incompressible elastic particle translating along the center line of a rigid cylindrical tube. When the particle surface and external boundary are in close proximity, the method of reflections converges poorly and a full numerical solution or further asymptotic reductions, for example, employing lubrication theory, are required to determine the fluid flow.

A large body of work has been concerned with the derivation of boundary conditions between a Stokes flow and a porous domain, rigid or deformable. Using simple experimental setups, different proposed boundary conditions can produce qualitatively similar macroscopic flow or deformation behaviours, making it difficult to differentiate them. This has led to various proposed conditions on the interface between the two domains [37–42]. Most recently, Xu *et al.* [43] derived three sets of interfacial conditions using a thermodynamic argument on energy dissipation. Several simple driving flows were used to compare each set with those previously derived by Minale [41]. In this work, we use boundary conditions similar to those employed by Ruiz-Baier *et al.* [44] and Badia *et al.* [45], and are summarized as the continuity of normal fluid flux, conservation of momentum, conservation of fluid normal stress, and the well-known Beavers and Joseph slip condition [37]. The originally empirical Beavers and Joseph slip condition (later theoretically justified by Saffman [38]) assumes a discontinuity in the tangential velocity across the interface that is proportional to the shear stress from the free fluid. We stress that it is not our aim to advocate for any one set of boundary conditions. On the contrary, our modeling framework is not limited to any particular choice of boundary conditions and, as a result, may be a powerful tool for exploring the validity of different boundary conditions.

The paper is structured as follows. In Sec. II we provide the governing equations and linearized boundary conditions describing the external Stokes flow and the linearly poroelastic particle. In Sec. III we present general solutions for the Stokes flow and linearly poroelastic particle, and calculate the fluid flow, the particle's translation and rotation, and resulting surface deformation given a general far-field flow. In Sec. IV we detail the two example far-field flows, shear flow and Poiseuille flow. For each case, we present and analyze closed-form solutions for the particle's velocity, rotation, and deformation, investigating the impacts of the permeability, slip, and the Poisson's ratio of the

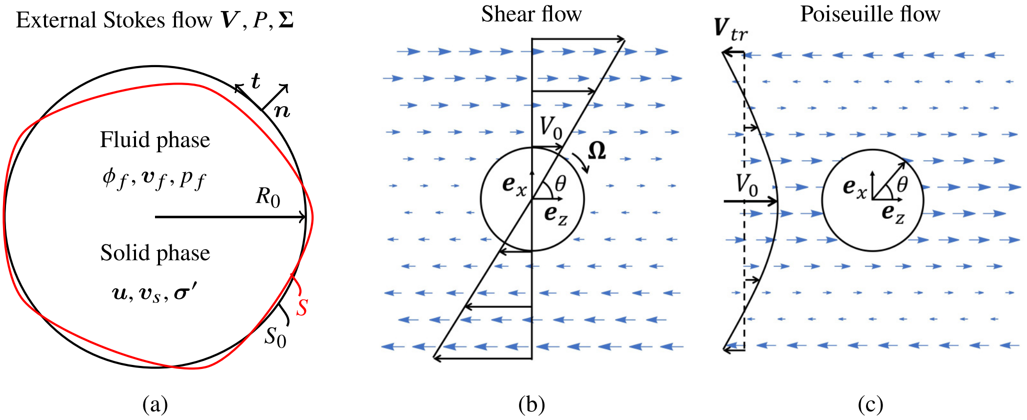

FIG. 1. (a) Poroelastic particle fully immersed in a Stokes flow. The particle is composed of a fluid and solid phase and has the undeformed and deformed boundaries S_0 and S, respectively. (b) Shear flow and (c) Poiseuille flow presented as far-field flows.

particle. By choosing limiting values of these parameters, we demonstrate exact agreement between our results and those obtained by Murata [30] for the case of an impermeable, incompressible elastic particle subject to no-slip boundary conditions. Finally, we provide closing discussions and outline future extensions in Sec. V.

II. GOVERNING EQUATIONS AND BOUNDARY CONDITIONS

We consider a three-dimensional, initially spherical, poroelastic particle of radius R_0 fully immersed in an incompressible viscous fluid as shown in Fig. 1. We assume the exterior flow is unbounded and driven solely by far-field conditions. The far-field conditions could reflect a flow involving an external boundary that is not explicitly considered here. We use spherical coordinates (r, θ, ϕ) with unit vectors $(\boldsymbol{e}_r, \boldsymbol{e}_\theta, \boldsymbol{e}_\phi)$ and align $r = 0$ with the center of the particle. Here $\theta \in [0, \pi)$ is the polar angle and $\phi \in [0, 2\pi)$ is the azimuthal angle. To avoid confusion, we present the transformation between the spherical and Cartesian coordinate systems in Appendix A. The undeformed particle boundary S_0 is defined as $r = R_0$. The deformed particle boundary is denoted by S. We assume the system is in equilibrium and work in a frame of reference that translates with the particle, noting that the particle's translational velocity in the laboratory frame is unknown and given by $\boldsymbol{V}_{tr}$. In this frame the particle rotates according to

$$\boldsymbol{v}_\Omega = r[\boldsymbol{\Omega} \times \boldsymbol{e}_r], \tag{2.1}$$

where $\boldsymbol{\Omega}$ remains to be determined.

In the analysis that follows, we assume the particle deformation is small such that the well-known equations of linear poroelasticity apply [46], and interfacial conditions are linearized onto the undeformed particle surface. For brevity, we present only the dimensionless linearized problem in the main text. This is additionally derived in the Supplemental Material [47] (Sec. I) as the leading-order asymptotic reduction of a nonlinear poroelastic particle in the small-deformation limit. To avoid confusion, all necessary quantities are defined both in both the main text and in the Supplemental Material such that each section is self-contained.

The nondimensionalization choices are summarized as follows. Lengths, velocities, and pressures/stresses are scaled on the particle radius R_0, the typical far-field velocity V_0 (see Fig. 1 for examples of V_0), and $\mu_f V_0/R_0$ where μ_f is the fluid viscosity, respectively. The dimensionless parameter

$$\epsilon = \frac{\mu_f V_0}{\mu_s R_0}, \tag{2.2}$$

where μ_s is the shear modulus of the particle, forms a scale for the solid strain. Here ϵ is defined as the ratio of typical viscous stresses in the external flow to the elastic stiffness of the solid skeleton. Finally, the deformation is scaled on ϵR_0. Assuming $\epsilon \ll 1$, we expect the solid strain and particle deformation to be small.

A. External flow

Neglecting inertial terms, the flow of external fluid is governed by the incompressible Stokes equations,

$$\nabla \cdot \boldsymbol{\Sigma} = \boldsymbol{0}, \tag{2.3}$$

$$\nabla \cdot \boldsymbol{V} = 0, \tag{2.4}$$

where $\boldsymbol{V}$ is the fluid velocity and $\boldsymbol{\Sigma}$ is the stress tensor for a Newtonian viscous fluid given by

$$\boldsymbol{\Sigma} = -P\boldsymbol{I} + [\nabla\boldsymbol{V} + (\nabla\boldsymbol{V})^T], \tag{2.5}$$

with P denoting the fluid pressure and the superscript T the transpose.

We calculate the leading-order net force $\boldsymbol{F}_{\text{force}}$ and torque $\boldsymbol{T}$ exerted on the particle by the surrounding fluid via the surface integrals

$$\boldsymbol{F}_{\text{force}} = \int_{\phi=0}^{2\pi} \int_{\theta=0}^{\pi} \boldsymbol{\Sigma}_{r=1} \cdot \boldsymbol{n}\ \sin\theta\ \mathrm{d}\theta\ \mathrm{d}\phi, \tag{2.6}$$

$$\boldsymbol{T} = \int_{\phi=0}^{2\pi} \int_{\theta=0}^{\pi} \boldsymbol{r} \times (\boldsymbol{\Sigma}_{r=1} \cdot \boldsymbol{n})\ \sin\theta\ \mathrm{d}\theta\ \mathrm{d}\phi, \tag{2.7}$$

where to leading order in ϵ we have $\boldsymbol{n} = \boldsymbol{e}_r$. For a particle in equilibrium with the surrounding flow we impose

$$\boldsymbol{F}_{\text{force}} = \boldsymbol{T} = \boldsymbol{0}, \tag{2.8}$$

from which we determine the particle's translational and angular velocities, $\boldsymbol{V}_{tr}$ and $\boldsymbol{\Omega}$, respectively.

B. Poroelastic particle

We assume the particle is composed of a porous and deformable solid skeleton (the solid phase) that is fully saturated by an interstitial fluid (the fluid phase) which is identical to the external fluid. We assume both phases are individually incompressible, though compression of the solid skeleton is permitted through local changes to the internal pore structure.

We begin by writing the porosity as

$$\phi_f = \phi_{f,0} + \epsilon(1 - \phi_{f,0})\nabla \cdot \boldsymbol{u}, \tag{2.9}$$

where $\phi_{f,0}$ is the initial volume fraction of fluid in the particle in its undeformed state which is assumed to be spatially constant, and $\boldsymbol{u}$ is the displacement of the solid skeleton.

Flow within the particle relative to the solid skeleton is governed by Darcy's law,

$$\phi_{f,0}(\boldsymbol{v}_f - \boldsymbol{v}_s) = -\tilde{\kappa}_0 \nabla p_f, \tag{2.10}$$

where $\boldsymbol{v}_f$ is the fluid velocity in the particle, $\boldsymbol{v}_s$ is the velocity of the solid skeleton, p_f is the pore/Darcy pressure, and the Darcy number $\tilde{\kappa}_0 = \kappa_0/R_0^2$, where $\kappa_0 = \kappa(\phi_{f,0})$ is the uniform permeability field associated with the initial porosity. In general the permeability will change as the solid skeleton deforms; however, under the assumption of small strain, we treat the permeability as constant [46]. The solid velocity is given by the rigid-body rotation

$$\boldsymbol{v}_s = \boldsymbol{v}_\Omega \tag{2.11}$$

since we seek steady solutions in a frame of reference that translates with the particle.

It will also be useful to define the total internal volumetric flux as

$$\boldsymbol{q} = \phi_{f,0}\boldsymbol{v}_f + (1 - \phi_{f,0})\boldsymbol{v}_s. \tag{2.12}$$

Imposing conservation of mass on the fluid and solid phases we have

$$\nabla \cdot \boldsymbol{v}_f = 0, \tag{2.13}$$

$$\nabla \cdot \boldsymbol{v}_s = 0, \tag{2.14}$$

where we note that since $\boldsymbol{v}_s$ is limited to the rigid body rotation Eq. (2.1), Eq. (2.14) is trivially satisfied.

To describe how the fluid and solid phases share internal stresses we write the total stress as

$$\boldsymbol{\sigma} = \boldsymbol{\sigma}' - p_f \boldsymbol{I}, \tag{2.15}$$

where $\boldsymbol{\sigma}'$ is Terzaghi's effective stress, which accounts for the elastic stress. It is defined as the force per unit area carried by the solid skeleton through deformation; details of this stress decomposition can be found in MacMinn *et al.* [46]. Under the assumption of small strain, we use a linear elastic constitutive relation for effective solid stress of the particle,

$$\boldsymbol{\sigma}' = \frac{2\nu}{1 - 2\nu}(\nabla \cdot \boldsymbol{u})\boldsymbol{I} + 2\boldsymbol{\varepsilon}, \tag{2.16}$$

where the Poisson's ratio ν measures the magnitude of transverse strain induced in the particle when deformed, and the small strain tensor $\boldsymbol{\varepsilon}$ is given by

$$\boldsymbol{\varepsilon} = \tfrac{1}{2}[\nabla \boldsymbol{u} + (\nabla \boldsymbol{u})^T]. \tag{2.17}$$

We note that the elastic constants ν and μ_s describe the mechanical properties of the solid skeleton and depend on both the skeleton material and its microstructure. At equilibrium we have

$$\nabla \cdot \boldsymbol{\sigma} = \nabla \cdot \boldsymbol{\sigma}' - \nabla p_f = \boldsymbol{0}. \tag{2.18}$$

C. Boundary conditions

Far from the particle we expect any disturbance to the external flow caused by the particle to be small such that

$$\boldsymbol{V} - \boldsymbol{V}_\infty - \boldsymbol{V}_{tr} \to 0 \quad \text{as} \quad r \to \infty, \tag{2.19}$$

where $\boldsymbol{V}_\infty$ and $\boldsymbol{V}_{tr}$ are the external far-field flow and particle's constant translational velocity in the laboratory frame, respectively. The deformed particle surface S is given by

$$\boldsymbol{r} = \boldsymbol{r}_s(\theta, \phi) = \boldsymbol{e}_r + \epsilon \boldsymbol{u}(r = 1). \tag{2.20}$$

Taking the modulus of Eq. (2.20) we approximate the surface deformation of the particle as

$$|\boldsymbol{r}_s(\theta, \phi)| \approx 1 + \epsilon\, \boldsymbol{u} \cdot \boldsymbol{e}_r|_{r=1}. \tag{2.21}$$

On the undeformed particle surface S_0, we impose the continuity of normal fluid flux, continuity of total stress, continuity of fluid stresses, and the Beavers and Joseph slip condition [37],

$$\boldsymbol{V}\cdot\boldsymbol{n}=\phi_{f,0}\boldsymbol{v}_f\cdot\boldsymbol{n}, \tag{2.22}$$

$$\boldsymbol{\Sigma}\cdot\boldsymbol{n}=\boldsymbol{\sigma}\cdot\boldsymbol{n}, \tag{2.23}$$

$$\boldsymbol{n}\cdot\boldsymbol{\Sigma}\cdot\boldsymbol{n}=-p_f, \tag{2.24}$$

$$\boldsymbol{t}^i\cdot\boldsymbol{\Sigma}\cdot\boldsymbol{n}=\tilde{\gamma}[(\boldsymbol{V}-\boldsymbol{q})\cdot\boldsymbol{t}^i], \tag{2.25}$$

where $\tilde{\gamma}=\gamma/\sqrt{\tilde{\kappa}_0}$ and the slip parameter γ is dependent on the material properties of the particle interface. For reference, $\gamma=0$ corresponds to a surface with perfect slip and $\gamma\to\infty$ corresponds to a surface with no slip. To avoid confusion, we note that in Young *et al.* [32] the slip parameter is instead defined as $\sqrt{\tilde{\kappa}_0}/\gamma$; however, in this work we remain consistent with Beavers and Joseph [37]. Here $\boldsymbol{n}=\boldsymbol{e}_r$, $\boldsymbol{t}^1=\boldsymbol{e}_\theta$, and $\boldsymbol{t}^2=\boldsymbol{e}_\phi$ are the normal and tangential unit vectors to the undeformed particle surface. These interfacial conditions form one of many viable choices [37,38,43,44]; the optimal choice of interfacial conditions will depend on the specific material choice and remains an active field of research [43]. By combining the interfacial conditions (2.23) and (2.24) we have the condition

$$\boldsymbol{n}\cdot\boldsymbol{\sigma}'\cdot\boldsymbol{n}=0, \tag{2.26}$$

which will be useful when calculating the particle deformation in Sec. III B.

III. METHOD OF SOLUTION

Under the assumption of small strain, the fluid problem given by (2.3)–(2.5), (2.8), (2.10), (2.13), (2.19), (2.22), (2.24), and (2.25) does not depend on the particle deformation, and reduces to flow through a rigid porous sphere. To determine the flow, we begin by prescribing the external flow in the absence of the particle, which is given by the far-field flow. This choice ensures the far-field condition (2.19) is satisfied. We then add a local correction due to the particle through the interfacial conditions (2.22), (2.24), and (2.25) where the internal flow is given by the solution to Eqs. (2.10) and (2.13).

Once the fluid problem is solved, the surface tractions and Darcy pressure drive the Navier-Láme problem Eqs. (2.18) and (2.16), which can be solved subject to the boundary conditions (2.23) and (2.26) to calculate the particle deformation. In Eq. (2.18), p_f is known from the fluid problem and is treated as a body force.

A. The fluid problem

We first consider the external Stokes flow ($r>1$), denoting the external velocity field in the absence of the particle by $\boldsymbol{V}^e$ and the local correction due to the particle by $\boldsymbol{V}^p$, such that

$$\boldsymbol{V}=\boldsymbol{V}^e+\boldsymbol{V}^p, \tag{3.1}$$

in the external fluid domain, with the corresponding pressure fields P^e and P^p.

The component $\boldsymbol{V}^e$ must satisfy Stokes equations (2.3)–(2.5) and the far-field condition (2.19) while remaining finite at the origin. Using the general solution in spherical coordinates derived by Lamb [48], we write

$$\boldsymbol{V}^e=\sum_{n=0}^{\infty}\left[\nabla\Phi_n*+\nabla\times(\boldsymbol{r}\Psi_n*)+\frac{n+3}{2(n+1)(2n+3)}r^2\nabla P_n*-\frac{n}{(n+1)(2n+3)}\boldsymbol{r}P_n*\right], \tag{3.2}$$

$$P^e=\sum_{n=0}^{\infty}P_n*, \tag{3.3}$$

where Φ_n*, Ψ_n* and P_n* are linear combinations of the regular solid spherical harmonics of degree n with constant coefficients as defined in Appendix B. To be clear, we write as an example

$$\Phi_n*(\boldsymbol{r}) = \sum_{m=-n}^{n} \Phi*_{n,m}\, \mathcal{R}_{n,m}(\boldsymbol{r}), \tag{3.4}$$

where $\mathcal{R}_{n,m}(\boldsymbol{r})$ are the regular solid spherical harmonics of degree n and order m and $\Phi*_{n,m}$ are the constant coefficients. The spherical harmonics Φ_n*, Ψ_n*, P_n* are calculated such that $\boldsymbol{V}^e = \boldsymbol{V}_\infty + \boldsymbol{V}_{tr}$.

The general solutions for the local correction to the flow and pressure fields, $\boldsymbol{V}^p$ and P^p, must decay as $r \to \infty$ in order to maintain the far-field condition Eq. (2.19). Hence, we find

$$\boldsymbol{V}^p = \sum_{n=1}^{\infty}\left[\nabla\Phi_{-n-1} + \nabla\times(\boldsymbol{r}\Psi_{-n-1}) - \frac{n-2}{2n(2n-1)}r^2\nabla P_{-n-1} + \frac{n+1}{n(2n-1)}\boldsymbol{r}P_{-n-1}\right], \tag{3.5}$$

$$P^p = \sum_{n=1}^{\infty} P_{-n-1}, \tag{3.6}$$

where Φ_{-n-1}, Ψ_{-n-1}, and P_{-n-1} are linear combinations of the irregular solid spherical harmonics of degree n. Again, we write as an example

$$\Phi_{-n-1}(\boldsymbol{r}) = \sum_{m=-n}^{n} \Phi_{n,m}\mathcal{I}_{n,m}(\boldsymbol{r}), \tag{3.7}$$

where $\mathcal{I}_{n,m}(\boldsymbol{r})$ are the irregular solid spherical harmonics and $\Phi_{n,m}$ are the constant coefficients. The total velocity and pressure fields are then obtained by adding the external background flow and local correction via Eq. (3.1). For clarity, the above general solutions for the velocity field and pressure all use a spherical coordinate system.

If we instead consider the internal flow ($r < 1$), combining (2.10), (2.11), and (2.13) we see the internal pore pressure satisfies Laplace's equation,

$$\nabla^2 p_f = 0. \tag{3.8}$$

Thus, keeping only terms which remain finite at the origin, has the general solution,

$$p_f = \sum_{n=0}^{\infty} p_n, \tag{3.9}$$

where p_n is a linear combination of the regular solid spherical harmonics of degree n, similar to Eq. (3.4). The internal flow is then given by Eq. (2.10).

The coefficients of the solid spherical harmonic functions Φ_{-n-1}, Ψ_{-n-1}, P_{-n-1}, and p_n are determined by the interfacial conditions (2.22), (2.24), and (2.25). It is convenient to rewrite these interfacial conditions in terms of radial components and derivatives,

$$V_r|_{r=1} = -\tilde{\kappa}_0 \left.\frac{\partial p_f}{\partial r}\right|_{r=1}, \tag{3.10}$$

$$\Sigma_{rr}|_{r=1} = -p_f|_{r=1}, \tag{3.11}$$

$$\left[r\frac{\partial \Sigma_{rr}}{\partial r} + 3(P + \Sigma_{rr})\right]_{r=1} = \tilde{\gamma}\left[r\frac{\partial V_r}{\partial r} + 2V_r + \tilde{\kappa}_0 r\frac{\partial^2 p_f}{\partial r^2} + 2\tilde{\kappa}_0 p_f\right]_{r=1}, \tag{3.12}$$

$$[\boldsymbol{r}\cdot\nabla\times(\boldsymbol{\Sigma}\cdot\boldsymbol{e}_r)]_{r=1} = [\boldsymbol{r}\cdot\nabla\times(\tilde{\gamma}\boldsymbol{V}) - \boldsymbol{r}\cdot\nabla\times(\tilde{\gamma}\boldsymbol{v}_s)]_{r=1}, \tag{3.13}$$

where Eqs. (3.12) and (3.13) are obtained by applying the divergence and curl operators to Eq. (2.25) and using Eqs. (2.4) and (2.3). For brevity, a derivation of this reformulation is omitted from the main text and is instead presented in the Supplemental Material [47] (Sec. II A). It is our hope that these details assist the interested reader who aims to rederive or extend the presented framework.

Substituting the general solutions for the Stokes velocity (3.2) and (3.5), Stokes pressure (3.3) and (3.6), and Darcy pressure (3.9) into (3.10)–(3.13) and applying the harmonic identities (B.8)–(B.10) we obtain a linear system of equations (presented for completeness in Sec. II A of the Supplemental Material [47]), which may be solved simultaneously at each degree $n \geqslant 0$ to give

$$\begin{aligned}\Phi_{-n-1} = {} & \frac{n(2n-1)\{2(n-1)n\tilde{\kappa}_0[2(n+2)\tilde{\kappa}_0+\tilde{\gamma}]-\tilde{\gamma}\}}{\omega}\Phi *_n \\ & + \frac{n(2n+1)\{n+1+2\tilde{\kappa}_0[3+(n-1)n(n+1)(n+2)]\}}{(n+1)(2n+3)\omega}P *_n \\ & - \frac{\tilde{\gamma}\{n+1-2\tilde{\kappa}_0[3+n(n^2-2n-6)]\}}{2(n+1)(2n+3)\omega}P *_n, \end{aligned} \tag{3.14}$$

$$\begin{aligned}P_{-n-1} = {} & \frac{2n(4n^2-1)\{2[2\tilde{\kappa}_0 n(n^2+n-2)-1]+\tilde{\gamma}[2\tilde{\kappa}_0(n-1)n-1]\}|}{\omega}\Phi *_n \\ & + \frac{n(2n-1)\{4\tilde{\kappa}_0 n(n^2+n-2)+\tilde{\gamma}[2\tilde{\kappa}_0(n^2-3n-1)-1]\}}{\omega}P *_n, \end{aligned} \tag{3.15}$$

$$p_n = -\frac{2n[4n^2-1)(2(n+2)+\tilde{\gamma}]}{\omega}\Phi *_n - \frac{(2n+1)(2[n^2-1)+(n-2)\tilde{\gamma}]}{\omega}P *_n, \tag{3.16}$$

$$\Psi_{-n-1} = \begin{cases} \dfrac{(n-1)-\tilde{\gamma}}{(n+2)+\tilde{\gamma}}\Psi *_n + \dfrac{2\tilde{\gamma}(\Omega^z\cos\theta+\Omega^x\cos\phi\sin\theta+\Omega^y\sin\theta\sin\phi)}{n(n+1)[(n+2)+\tilde{\gamma}]}, & n = 1, \\ \dfrac{(n-1)-\tilde{\gamma}}{(n+2)+\tilde{\gamma}}\Psi *_n, & n \neq 1, \end{cases} \tag{3.17}$$

where

$$\omega = 2(\{1+n[2n+3+2\tilde{\kappa}_0(n+2)(2n^2+1)]\}+\tilde{\gamma}[n+1+\tilde{\kappa}_0 n(1+2n^2)]). \tag{3.18}$$

In Eq. (3.17), Ω^x, Ω^y, Ω^z are the z, y, and z components of the particle's rotation $\boldsymbol{\Omega}$.

We remind the reader that $\Phi *_n$, $P *_n$, and $\Psi *_n$ are determined by the external flow $\boldsymbol{V}^e$ through the far-field condition (2.19) which contains the particle's unknown translational velocity $\boldsymbol{V}_{tr}$. To calculate the particle's translational velocity, along with its rotational velocity $\boldsymbol{\Omega}$, we enforce the balances of linear and angular momentum (2.8). Substituting the solid spherical harmonic representation for $\boldsymbol{\Sigma}$ into Eqs. (2.6) and (2.7) we find

$$F^x = -4\pi P_{-2,1}, \quad F^y = -4\pi P_{-2,-1}, \quad F^z = -4\pi P_{-2,0}, \tag{3.19}$$

$$T^x = -8\pi \Psi_{-2,1}, \quad T^y = -8\pi \Psi_{-2,-1}, \quad T^z = -8\pi \Psi_{-2,0}, \tag{3.20}$$

where the superscripts x, y, and z again denote the x, y and z components, respectively. Consequently, to satisfy Eq. (2.8) we have the further conditions

$$P_{-2,m} = 0, \quad \Psi_{-2,m} = 0, \quad m = 0, \pm 1, \tag{3.21}$$

which allow the relationship between the external flow and the particle's translation/rotation to be determined. The full solution for the fluid problem is given by combining Eq. (3.21) with (3.14)–(3.17).

B. The solid problem

The general solution to the Navier-Láme problem in three dimensions may be written using the Papkovich-Neuber potentials [49],

$$2\boldsymbol{u} = 2(1-\nu)\boldsymbol{\psi} - \nabla\left(\varphi + \frac{1}{2}\boldsymbol{r}\cdot\boldsymbol{\psi}\right), \tag{3.22}$$

where φ and $\boldsymbol{\psi}$ satisfy the Poisson equations,

$$\nabla^2\boldsymbol{\psi} = \frac{\nabla p_f}{1-\nu} \qquad \text{and} \qquad \nabla^2\varphi = -\frac{\boldsymbol{r}\cdot\nabla p_f}{2(1-\nu)}. \tag{3.23}$$

We decompose φ and $\boldsymbol{\psi}$ into their complementary and particular components by writing

$$\varphi = \varphi_c + \varphi_p \qquad \text{and} \qquad \boldsymbol{\psi} = \boldsymbol{\psi}_c + \boldsymbol{\psi}_p, \tag{3.24}$$

where φ_c and $\boldsymbol{\psi}_c$ satisfy the homogeneous problem and φ_p and $\boldsymbol{\psi}_p$ are the particular solutions for the inhomogeneities in Eq. (3.23).

We first consider the particular solutions to Eq. (3.23). Since p_f is harmonic, it may be shown that ∇p_f is also harmonic. Applying the identity (B9) with $l = 2$, and using Eq. (3.9), we obtain exact expressions for the particular solutions,

$$\varphi_p(\boldsymbol{r}) = -\frac{r^2}{2(1-\nu)}\sum_{n=0}^{\infty}\frac{np_n}{2(2n+3)}, \tag{3.25}$$

$$\boldsymbol{\psi}_p(\boldsymbol{r}) = \frac{r^2}{1-\nu}\sum_{n=0}^{\infty}\frac{\nabla p_n}{2(2n+3)}. \tag{3.26}$$

We now consider the complimentary solutions to Eq. (3.23). Within a spherical domain, we may set $\varphi_c = 0$ without loss of generality using the Papkovich-Neuber representation [50]. Studying Eq. (3.23), we see that the components of $\boldsymbol{\psi}_c$ are harmonic and remain finite at the origin. Using Appendix B we write their explicit forms as

$$\boldsymbol{\psi}_c(\boldsymbol{r}) = \sum_{n=0}^{\infty}\boldsymbol{\psi}_n(\boldsymbol{r}) = \sum_{n=0}^{\infty}\sum_{m=-n}^{n}\boldsymbol{\psi}_{n,m}\mathcal{R}_{n,m}(\boldsymbol{r}), \tag{3.27}$$

where again $\mathcal{R}_{n,m}(\boldsymbol{r})$ are the regular solid spherical harmonics, and $\boldsymbol{\psi}_n$ are linear combinations of the regular solid spherical harmonics of degree n with the constant coefficients $\boldsymbol{\psi}_{n,m}$ as presented in Eq. (B6).

To calculate the solid displacement, it remains to calculate the constant coefficients $\boldsymbol{\psi}_{n,m}$ via the boundary conditions Eqs. (2.23) and (2.26). We again reformulate these boundary conditions by applying the divergence and curl to Eq. (2.23) to obtain

$$\sigma'_{rr}|_{r=1} = 0, \tag{3.28}$$

$$\left[r\frac{\partial p_f}{\partial r} + (3\lambda + 2\mu_s)(\nabla\cdot\boldsymbol{u}) - r\frac{\partial\sigma'_{rr}}{\partial r} - 3p_f\right]_{r=1} = -\left[3P + r\frac{\partial\Sigma_{rr}}{\partial r}\right]_{r=1}, \tag{3.29}$$

$$[\boldsymbol{r}\cdot\nabla\times(\boldsymbol{\sigma}'\cdot\boldsymbol{e}_r)]_{r=1} = [\boldsymbol{r}\cdot\nabla\times(\boldsymbol{\Sigma}\cdot\boldsymbol{e}_r)]_{r=1}, \tag{3.30}$$

with a derivation of the reformulation provided in the Supplemental Material [47] (Sec. II B).

Substituting the Papkovich-Neuber representation for the solid displacement (3.22) into the boundary conditions (3.28)–(3.30) we obtain

$$\sum_{n=0}^{\infty}\frac{1}{2}(3-4\nu-n)n[\boldsymbol{r}\cdot\boldsymbol{\psi}_c]_n + \nu[\nabla\cdot\boldsymbol{\psi}_c]_n + \left(\frac{n+4}{4} - \nu(n+1)\right)\frac{1}{1-\nu}\frac{np_n}{2n+3} = 0, \tag{3.31}$$

$$\begin{aligned}
&\sum_{n=0}^{\infty}(n-3)p_n + (1+\nu)([\boldsymbol{r}\cdot\boldsymbol{\psi}_c]_n - \nu(n-1)[\nabla\cdot\boldsymbol{\psi}_c]_n - \frac{1}{2}(3-4\nu-n)n(n-1)[\boldsymbol{r}\cdot\boldsymbol{\psi}_c]_n \\
&\quad + \left[1+\nu-(n+1)\left(\frac{n+2}{4}-\nu(n+1)\right)\right]\frac{1}{1-\nu}\frac{np_n}{2n+3} \\
&= -\sum_{n=0}^{\infty}\left[2n(n-1)(n-2)\Phi *_n + \frac{(n^2-n-3)n}{2n+3}P *_n - 2(n+1)(n+2)(n+3)\Phi_{-n-1}\right. \\
&\quad \left. + \frac{(n^2+3n-1)(n+1)}{2n-1}P_{-n-1} + 3(P *_n + P_{-n-1})\right], \qquad (3.32)
\end{aligned}$$

$$\sum_{n=0}^{\infty}[(1-\nu)(n-1)[\boldsymbol{r}\times\boldsymbol{\psi}_c]_n = \sum_{n=0}^{\infty}[n(n+1)(n-1)\Psi *_n - n(n+1)(n+2)\Psi_{-n-1}]. \qquad (3.33)$$

When solving the above boundary conditions (3.31)–(3.33) to calculate the constant coefficients $\boldsymbol{\psi}_{n,m}$, it is convenient to use a Cartesian basis. This is because each of the Cartesian components of $\boldsymbol{\psi}$ (hereafter denoted as ψ_c^x, ψ_c^y, and ψ_c^z) satisfies Laplace's equation and is thus harmonic. For clarity, we write

$$\boldsymbol{\psi}_c^x(\boldsymbol{r}) = \boldsymbol{\psi}_c(\boldsymbol{r})\cdot\boldsymbol{e}_x = \sum_{n=0}^{\infty}\boldsymbol{\psi}_n^x(\boldsymbol{r}) = \sum_{n=0}^{\infty}\sum_{m=-n}^{n}\boldsymbol{\psi}_{n,m}^x\mathcal{R}_{n,m}(\boldsymbol{r}), \qquad (3.34)$$

with similar expressions for the y and z components of $\boldsymbol{\psi}_c$. The divergence, gradient, and cross-product terms present in (3.31)–(3.33) are then written as

$$[\boldsymbol{r}\cdot\boldsymbol{\psi}_c]_n = x\psi_n^x + y\psi_n^y + z\psi_n^z, \quad [\nabla\cdot\boldsymbol{\psi}_c]_n = \frac{\partial\psi_n^x}{\partial x} + \frac{\partial\psi_n^y}{\partial y} + \frac{\partial\psi_n^z}{\partial z}, \qquad (3.35)$$

$$[\boldsymbol{r}\times\boldsymbol{\psi}_c]_n = y\frac{\partial\psi_n^x}{\partial z} - z\frac{\partial\psi_n^x}{\partial y} + z\frac{\partial\psi_n^y}{\partial x} - x\frac{\partial\psi_n^y}{\partial z} + x\frac{\partial\psi_n^z}{\partial y} - y\frac{\partial\psi_n^z}{\partial x}, \qquad (3.36)$$

respectively. Unlike in the fluid problem, the system of equations obtained by substituting Eqs. (3.35) and (3.36), into (3.31)–(3.33) is not diagonal and cannot be solved simultaneously at each degree n and order m. This is due to the terms

$$\begin{gathered}
\frac{\partial\psi_n^x}{\partial x}, \quad \frac{\partial\psi_n^y}{\partial y}, \quad \frac{\partial\psi_n^z}{\partial z}, \quad x\psi_n^x, \quad y\psi_n^y, \quad z\psi_n^z, \\
z\frac{\partial\psi_n^x}{\partial y}, \quad y\frac{\partial\psi_n^x}{\partial z}, \quad z\frac{\partial\psi_n^y}{\partial x}, \quad x\frac{\partial\psi_n^y}{\partial z}, \quad x\frac{\partial\psi_n^z}{\partial y}, \quad y\frac{\partial\psi_n^z}{\partial x}, \qquad (3.37)
\end{gathered}$$

which are not orthogonal with the solid spherical harmonic of degree n. To overcome this, we first project these terms to a solid spherical harmonic basis by writing, for example,

$$\begin{aligned}
\frac{\partial\psi_n^x}{\partial x} &= \sum_{n=0}^{\infty}\sum_{m=-n}^{n}\left[\int_{\phi=0}^{2\pi}\int_{\theta=0}^{\pi}\frac{(2n+1)}{4\pi r^{2n}}\frac{\partial\psi_n^x}{\partial x}\mathcal{R}_{n,m}(r,\theta,\phi)\ \sin\theta\ \mathrm{d}\theta\ \mathrm{d}\phi\right]\mathcal{R}_{n,m}(r,\theta,\phi) \\
&= \sum_{n=0}^{\infty}\sum_{m=-n}^{n}\widetilde{\psi}_{n,m}^x\mathcal{R}_{n,m}(r,\theta,\phi), \qquad (3.38)
\end{aligned}$$

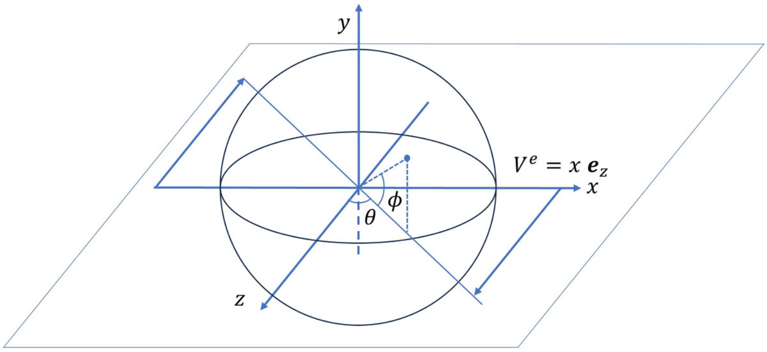

FIG. 2. Detailed schematic of a poroelastic particle under a shear flow. Details of the transformation between the spherical and Cartesian coordinate systems are presented in Appendix A.

where $\widetilde{\psi}^x_{n,m}$ are projected constants, and we note that

$$\frac{\partial \psi^x_c}{\partial x} = \sum_{n=0}^{\infty} \frac{\partial \psi^x_n}{\partial x}. \tag{3.39}$$

Projections for the remaining terms in Eq. (3.37) can similarly be calculated. On the particle boundary ($r = 1$), the projected constants (for example, $\widetilde{\psi}^x_{n,m}$) are simply linear combinations of the unknown coefficients $\psi^x_{n,m}$, $\psi^y_{n,m}$, and $\psi^z_{n,m}$. Importantly, the sums for the projections all involve a finite number of terms. Therefore, by substituting Eq. (3.38), along with similar projections for the remaining terms in Eq. (3.37) into the boundary conditions (3.31)–(3.33) we may exploit the orthogonality of the spherical harmonics and solve (3.31)–(3.33) exactly by formulating a nondiagonal, finite-dimensional linear system in terms of the coefficients $\psi^x_{n,m}$, $\psi^y_{n,m}$, and $\psi^z_{n,m}$. For the sake of brevity the full solution is omitted from the text; however, we do provide an implementation of this method in *Mathematica* in the Supplemental Material [47]. Once the constants $\psi^x_{n,m}$, $\psi^y_{n,m}$, and $\psi^z_{n,m}$ are calculated, we use the Papkovich-Neuber representation (3.22) to predict the surface displacement (2.21). The impact of the particle deformation on the porosity may be calculated via Eq. (2.9), completing the solid problem.

IV. EXAMPLE FLOW PROFILES

We use the above framework to investigate the impacts of the Darcy number, slip, and Poisson's ratio on the particle's translational and angular velocity, and its surface deformation for two example flow profiles, shear flow, and Poiseuille flow. By taking the limits $\tilde{\kappa}_0 \to 0$, $\gamma \to \infty$, and $\nu \to 1/2$ we model an incompressible, elastic particle subject to no-slip boundary conditions in an unbounded flow as studied by Murata [30]. [1] For both background flows, we apply these limits to our solutions and compare to Murata to provide validation to the method.

A. Shear flow

We first study the impact of shear flow on a poroelastic particle, as presented in Fig. 2. In a Cartesian coordinate system, the dimensionless background shear flow is described by

$$\boldsymbol{V}^e = x\boldsymbol{e}_z. \tag{4.1}$$

---

[1] Taking these limits, the Darcy pressure does not reduce to the elastic pressure in the particle. Further details of this reduction are provided in Appendix C.

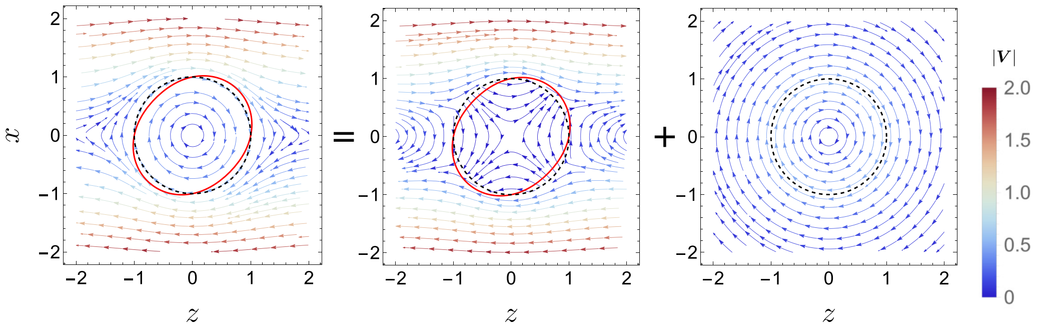

(a) Shear flow

(b) No particle rotation and background shear flow

(c) Pure particle rotation and zero background flow

FIG. 3. Streamline plots in the z-x plane ($y = 0$) showing an internal and external flow fields. (a) A particle rotating under shear flow can be expressed as the superposition of (b) a nonrotating particle under shear flow and (c) a rotating particle in the absence of external flow. In all plots $\tilde{\kappa}_0 = 0.001$ and $\gamma = 100$. The undeformed and deformed ($\epsilon = 0.1$, $\nu = 0.25$) particle surface are denoted by the black dashed and red lines, respectively.

We first write the external background flow using solid spherical harmonics,

$$\Psi*_1 = -\tfrac{1}{2} r \sin\theta \sin\phi, \tag{4.2}$$

$$\Phi*_2 = \tfrac{1}{4} r^2 \sin 2\theta \cos\phi. \tag{4.3}$$

From Eq. (3.21) it can be shown that the translational velocity of the particle $\boldsymbol{V}_{tr} = \boldsymbol{0}$, and that the torque balance requires

$$\frac{\tilde{\gamma}(2 + 4\Omega^y)}{4(3 + \tilde{\gamma})} = 0, \tag{4.4}$$

such that the particle rotates according to

$$\Omega^x = \Omega^z = 0, \quad \Omega^y = -\tfrac{1}{2}. \tag{4.5}$$

The first term in Eq. (4.4) is the torque imposed on a nonrotating particle under a shear flow [see, for example, Fig. 3(b)], and the second term in Eq. (4.5) is the torque required to generate the particle rotation Ω^y [see, for example, Fig. 3(c)]. Since these contributions scale identically with $\tilde{\kappa}_0$ and γ, the particle rotation is constant. Special attention must be paid to the case when $\gamma = \tilde{\gamma} = 0$, such that there is perfect slip on the particle surface. This case forms a singular limit where $\boldsymbol{\Omega} = \boldsymbol{0}$ is not uniquely determined. However, we note that $\boldsymbol{\Omega} = -\boldsymbol{e}_y/2$ in the limit as $\tilde{\gamma} \to 0$.

We then predict the surface deformation,

$$r_s = 1 + \frac{5}{4}\epsilon L^s(\tilde{\kappa}_0, \tilde{\gamma}, \nu) \sin 2\theta \cos\phi,$$
$$L^s(\tilde{\kappa}_0, \tilde{\gamma}, \nu) = \frac{16(2+\nu) + \tilde{\gamma}(4 + 11\nu)}{(5 + 48\tilde{\kappa}_0 + \tilde{\gamma} + 6\tilde{\kappa}_0\tilde{\gamma})(7 + 5\nu)}, \tag{4.6}$$

where $L \in [0, 1]$ contains the dependencies of the surface deformation on $\tilde{\kappa}_0$, $\tilde{\gamma}$, and ν. Although $\tilde{\gamma}$ appears in the solutions, it is important to recall that $\tilde{\gamma} = \gamma/\sqrt{\tilde{\kappa}_0}$ is composed of two independent and physically meaningful parameters, and we choose to explore how γ and $\tilde{\kappa}_0$ impact the system rather than $\tilde{\gamma}$. By taking the limits $\nu \to 1/2$ (incompressible), $\gamma \to \infty$ (no-slip), and $\tilde{\kappa}_0 \to 0$ (impermeable), we see that $L^s(\tilde{\kappa}_0, \tilde{\gamma}, \nu) \to 1$. In this limit, we exactly recover the surface deformation predicted by Murata [30] for an incompressible, impermeable elastic particle in shear flow subject to no-slip boundary conditions. The rigid body rotation of the particle given by Eq. (4.5) is identical

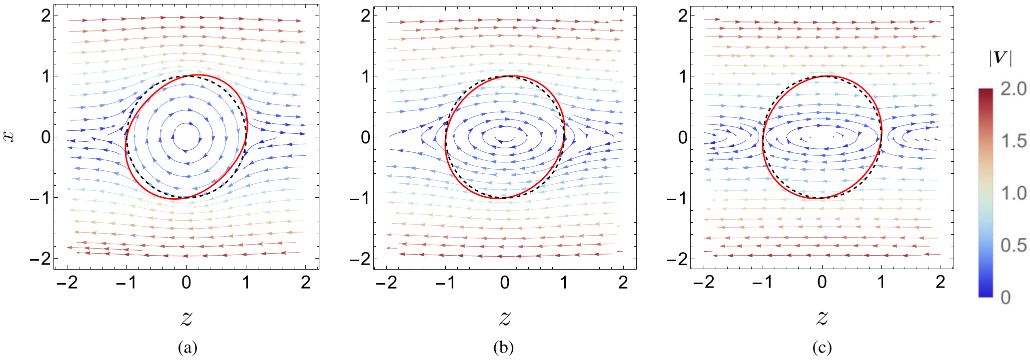

FIG. 4. Streamline plots in the z-x plane for a poroelastic particle in shear flow varying $\tilde{\kappa}_0$ and γ for $y = 0$. In (a) $(\tilde{\kappa}_0, \gamma) = (0.001, 0.01)$, (b) (0.1, 100), and (c) (0.1, 0.01). The undeformed and deformed ($\epsilon = 0.1$, $\nu = 0.25$) particle surface are denoted by the black dashed and red lines, respectively.

to Murata's result regardless of the parameter choices. We also note that the particle rotation is identical to that predicted by Young *et al.* [32] using different interfacial conditions.

In Fig. 3 we choose a small Darcy number $\tilde{\kappa}_0 = 0.001$ and small slip $\gamma = 100$, presenting a streamline plot in the z-x plane for the poroelastic particle [Fig. 3(a)] as a linear combination of the shear flow through a stationary nonrotating particle [Fig. 3(b)], and the flow associated with a rotating particle in a stationary fluid [Fig. 3(c)]. Outside the particle we plot the velocity field $\boldsymbol{V}$ and inside the particle we plot the total volume flux $\boldsymbol{q}$. In each plot, the streamline color reflects the velocity magnitude. In Fig. 3(b) where the particle does not rotate, the internal flow is extensional along a 45° angle to the flow, which we define as the major axis. We also define the minor axis as perpendicular to the major axis in the z-x plane. We note the streamlines cross the z axis as a result of the particle; with no particle the background flow has a line of stagnation points along $x = 0$. With small slip ($\gamma = 100$), the pure rotation of the particle in Fig. 3(c) causes the external flow to circle the particle. The total internal flux $\boldsymbol{q}$ is given exactly by the rotation (4.5) and the external flow decays to zero far from the particle. Since there is no normal flow present in Fig. 3(c), the Darcy number $\tilde{\kappa}_0$ affects only the external flow through the Beavers and Joseph condition (2.25) via the parameter $\tilde{\gamma} = \gamma/\sqrt{\tilde{\kappa}_0}$. With a smaller Darcy number, $\tilde{\gamma}$ is increased, reducing the slip on the particle surface such that the particle rotation generates a greater external flow. Combining the streamlines in Figs. 3(b) and 3(c), we obtain Fig. 3(a). Since the Darcy number is small here, the internal flow is dominated by the particle rotation such that we observe circular streamlines. Due to the small slip, the external flow close to the particle boundary is dominated by the rotation such that the flow across the z axis observed in Fig. 3(b) changes direction and the external flow circles the particle. Far from the particle we recover the background shear flow.

Since no surface deformation is generated via the particle rotation, the deformed surfaces, presented via the red lines, are identical in Figs. 3(b) and 3(c). Unsurprisingly, the particle deforms to a prolate spheroid aligned with the major axis of the extensional internal flow in Fig. 3(b).

In Fig. 4 we present further 2D cross sections (x-z plane) of the streamlines and surface deformation under a shear flow for varying Darcy number and slip. In Fig. 4(a) the Darcy number is again small such that there is little internal fluid flow relative to the rotating skeleton. Consequently, the internal streamlines are near circular reflecting the particle rotation in Eq. (4.5). Comparing with Fig. 3(a), with a large slip ($\gamma = 0.01$) the external flow does not circle the particle, since the rotation of the particle generates little external flow. We note that the flow around the particle is faster since the greater slip reduces the resistance to tangential flow. In Figs. 4(b) and 4(c) we increase the Darcy number and observe ellipsoidal internal flow due to the increased internal flow relative to the particle rotation. With a small slip in Fig. 4(b) the external flow mimics the ellipsoidal internal flow near the interface. With a large slip (γ small) in Fig. 4(c) the particle rotation does not generate a

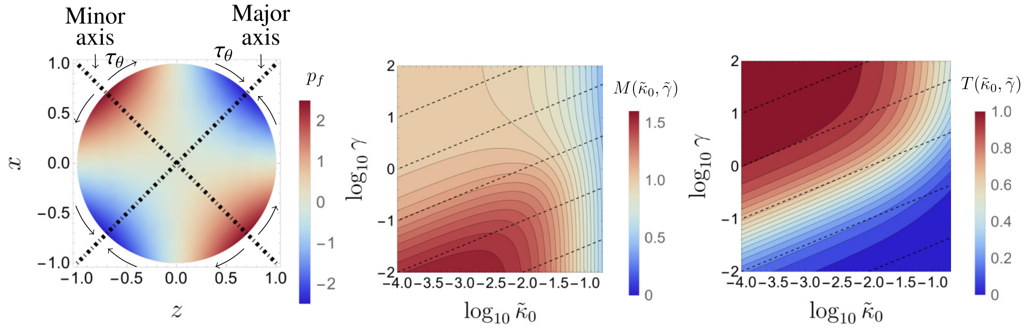

(a) (b) (c)

FIG. 5. (a) Darcy pressure p_f within the particle for $\tilde{\kappa}_0 = 0.001$ and $\gamma = 100$ with $y = 0$. (b) Dependence of the Darcy pressure on $\tilde{\kappa}_0$ and γ, $M^s(\tilde{\kappa}_0, \tilde{\gamma})$. (c) Dependence of the surface shearing traction on $\tilde{\kappa}_0$ and γ, $T^s(\tilde{\kappa}_0, \tilde{\gamma})$. In (b) and (c) the dashed lines are lines of fixed $\tilde{\gamma}$ and vary from 10^{-1} to 10^3 in powers of 10.

strong external flow such that we see a similar external flow structure to that observed in Fig. 3(b) when rotation is neglected. We note that the flow in Fig. 4(a) is similar to that presented in Fig. 4(c), though the flow through the xz axis is too subtle to be visible in the streamline plot. In all cases, far from the particle we recover the far-field shear flow with horizontal streamlines. The streamlines around $x = 2$ in Figs. 3(a) and 4(a)–4(c) are in general more strongly curved for a smaller Darcy number and slip, which indicates the disturbance to the flow is larger.

For all cases in Fig. 4, the particle attains a similar prolate spheroidal shape to that observed in Fig. 3. To interpret the surface deformation in Eq. (4.6), we consider the surface tractions, $\boldsymbol{\tau} = \boldsymbol{\Sigma} \cdot \boldsymbol{n}(r = 1)$ and the Darcy pressure, both of which force the resulting particle deformation. Under an external shear flow we have

$$p_f = -\frac{5}{2} M^s(\tilde{\kappa}_0, \tilde{\gamma}) r^2 \sin 2\theta \cos\phi, \tag{4.7}$$

$$\boldsymbol{\tau} \cdot \boldsymbol{e}_\theta = \frac{5}{2} T^s(\tilde{\kappa}_0, \tilde{\gamma}) \cos 2\theta \cos\phi, \qquad \boldsymbol{\tau} \cdot \boldsymbol{e}_\phi = -\frac{5}{2} T^s(\tilde{\kappa}_0, \tilde{\gamma}) \cos\theta \cos\phi, \tag{4.8}$$

where

$$M^s(\tilde{\kappa}_0, \tilde{\gamma}) = \left(\frac{8}{\tilde{\gamma}} + 1\right) T^s(\tilde{\kappa}_0, \tilde{\gamma}), \qquad T^s(\tilde{\kappa}_0, \tilde{\gamma}) = \frac{\tilde{\gamma}}{5 + 48\tilde{\kappa}_0 + \tilde{\gamma} + 6\tilde{\kappa}_0\tilde{\gamma}},$$

where M and T contain the dependencies on $\tilde{\kappa}_0$ and $\tilde{\gamma}$ and are such that $M^s(\tilde{\kappa}_0, \tilde{\gamma}) \to 1$ and $T^s(\tilde{\kappa}_0, \tilde{\gamma}) \to 1$ for the case of an incompressible, no-slip, impermeable elastic particle.

In Fig. 5 we present an example plot of the Darcy pressure within the particle with $\tilde{\kappa}_0 = 0.001$ and $\gamma = 100$, along with $M^s(\tilde{\kappa}_0, \tilde{\gamma})$ and $T^s(\tilde{\kappa}_0, \tilde{\gamma})$. For reference, in Fig. 5(a) we also present the major and minor axes, along with the direction of the surface shearing traction $\tau_\theta = \boldsymbol{\tau} \cdot \boldsymbol{e}_\theta$. In Fig. 5(a) we see that the Darcy pressure is negative along the major axis and positive along the minor axis, mimicking the extensional internal streamlines presented in Fig. 3(b). The Darcy pressure absorbs the normal surface traction through the interfacial condition (2.24) and generates deformation of the solid skeleton via the momentum equation (2.15). Since a positive pressure indicates compression and a negative pressure indicates extension, the Darcy pressure acts to stretch the solid skeleton along the major axis and compress it along the minor axis. Instead, considering the shearing tractions in Eq. (4.8) with $y = 0$, we have $\tau_\phi = 0$ and τ_θ involves compression of the particle toward the major axis and stretching away from the minor axis, as indicated by the curved arrows near the particle surface. We present the dependencies of M and T on the Darcy number and slip in Figs. 5(b) and 5(c), observing that the Darcy pressure/normal surface traction magnitude

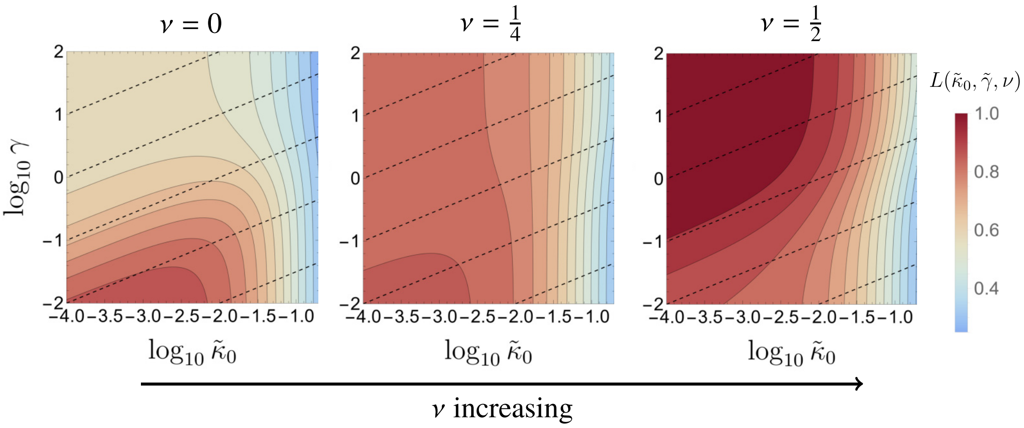

FIG. 6. Contour plots of the magnitude of the particle surface deformation, $L^s(\tilde{\kappa}_0, \tilde{\gamma}, \nu)$. We continuously vary $\tilde{\kappa}_0$ and γ for $\nu = 0, 1/4, 1/2$. The dashed lines are lines of fixed $\tilde{\gamma}$ and vary from 10^{-1} to 10^3 in powers of 10.

decrease with increasing γ for fixed $\tilde{\kappa}_0$ and that the shearing fluid tractions increase with increasing γ for fixed $\tilde{\kappa}_0$. With a larger slip (smaller γ), the external flow is increased, as was observed in Figs. 3(a) and 4(a). This increase in the external flow leads to a greater magnitude of the normal surface traction, and hence Darcy pressure.

Increasing the Darcy number has two effects. First, a greater internal fluid flow is permitted which reduces the flow which is diverted around the particle. This effect decreases both the Darcy pressure and the surface shearing traction. Second, through Eq. (2.25) increasing the Darcy number decreases $\tilde{\gamma} = \gamma/\sqrt{\tilde{\kappa}_0}$, which effectively increases the slip on the particle surface. This has the effect of increasing the Darcy pressure and further decreasing the surface shearing traction. The combination of these two effects is evident in Fig. 5(b) where increasing the Darcy number for small γ initially increases the pressure due to the effective reduction in slip via Eq. (2.25) until the Darcy number $\tilde{\kappa}_0 \sim 0.01$. When γ is larger, increasing the Darcy number only ever decreases M, since $\tilde{\gamma}$ remains large for all $\tilde{\kappa}_0$. If we instead consider the lines of constant $\tilde{\gamma}$ (dashed lines) in Figs. 5(b) and 5(c), the Darcy pressure and surface shearing traction only decrease with $\tilde{\kappa}_0$ since the effect of the Darcy number on slip is removed. This may be verified by inspecting the closed form solutions for M and T in Eq. (4.8), where $\tilde{\kappa}_0$ appears explicitly in the denominator. For small $\tilde{\kappa}_0$, the contours are parallel to the lines of constant $\tilde{\gamma}$. With a small Darcy number, the effect of the increased internal flow is minimal such that the Darcy pressure and surface shearing tractions depend predominantly on $\tilde{\gamma}$.

The combination of these forcing effects has nontrivial implications for the predicted surface deformation of the particle (4.6). In Fig. 6 we present contour plots of $L^s(\tilde{\kappa}_0, \tilde{\gamma}, \nu)$, varying the Darcy number and slip for three values of the Poisson's ratio. When $\nu = 0$ no transverse strains are developed when the particle is deformed. In this case, the shearing fluid traction presented in Eq. (4.8), which compresses the particle toward the major axis and away from the minor axis, cannot cause the particle to deform from a sphere. Consequently, only the Darcy pressure contributes to the resulting surface deformation such that the surface deformation magnitude has identical dependencies to $M^s(\tilde{\kappa}_0, \tilde{\gamma})$ as presented in Fig. 5(b). When $\nu = 1/2$, the particle is incompressible and the maximal transverse strains are induced when the particle is deformed. In this case, the shearing surface traction generates a transverse deformation which is positive along the major axis and negative along the minor axis. Consequently, the resulting surface deformation given by Eq. (2.20) is due to a combination of both the Darcy pressure and the transverse strains generated by the surface shearing traction. In this case, the surface deformation is dominated by the surface

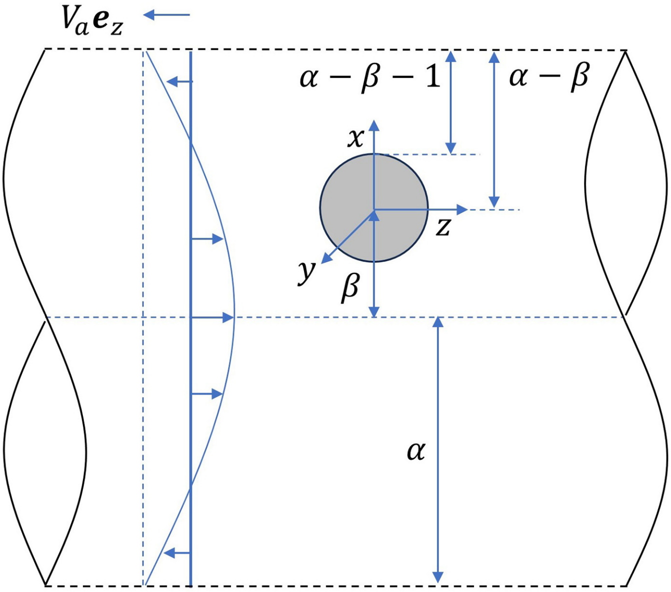

FIG. 7. Schematic of a poroelastic particle under Poiseuille flow in a frame of reference that translates with the particle. The particle has unit radius, the tube radius is α, and the particle is a distance β from the tube center line. The tube walls move with velocity $-V_a\boldsymbol{e}_z = \boldsymbol{V}_{tr}$, corresponding to the translational velocity of the particle in the laboratory frame.

shearing traction and we observe that, in contrast to when $\nu = 0$, $L^s(\tilde{\kappa}_0, \tilde{\gamma}, 1/2)$ increases with γ as was observed with $T^s(\tilde{\kappa}_0, \tilde{\gamma})$ as presented in Fig. 5(c). When $\nu = 1/4$ we observe that the surface deformation magnitude increases with γ when the Darcy number is large, and decreases with γ when the Darcy number is small. The Poisson's ratio therefore details the extent to which the shearing traction contributes to the resulting surface deformation. This interpretation motivates the decomposition

$$L^s(\tilde{\kappa}_0, \tilde{\gamma}, \nu) = \frac{2(2+\nu)}{7+5\nu} M^s(\tilde{\kappa}_0, \tilde{\gamma}) + \frac{9\nu}{7+5\nu} T^s(\tilde{\kappa}_0, \tilde{\gamma}), \tag{4.9}$$

where we can see clearly that when $\nu = 0$, the shear stress T^s does not contribute to the resulting surface deformation, and when $\nu = 1/2$, contributes maximally to the dependencies on $\tilde{\kappa}_0$ and $\tilde{\gamma}$.

B. Poiseuille flow

Figure 7 presents the problem schematic for a poroelastic particle translating in a cylindrical tube using a coordinate system that translates with the center of the particle. Here α is the tube radius, the particle is a distance β from the tube center line, and the wall velocity $V_a\boldsymbol{e}_z = \boldsymbol{V}_{tr}/V_0$ is the normalized translational velocity of the particle in the laboratory frame. We note that the tube walls are represented by dashed lines, since they are not explicitly considered in the solution framework. In order for the solution framework to remain valid, the particle must be sufficiently far from the tube wall. We therefore require

$$\alpha - \beta - 1 = O(1), \tag{4.10}$$

such that the particle does not disrupt the flow on the tube wall too strongly. In Figs. 8–10, we choose $\alpha = 2$ and $\beta = 1/3$.

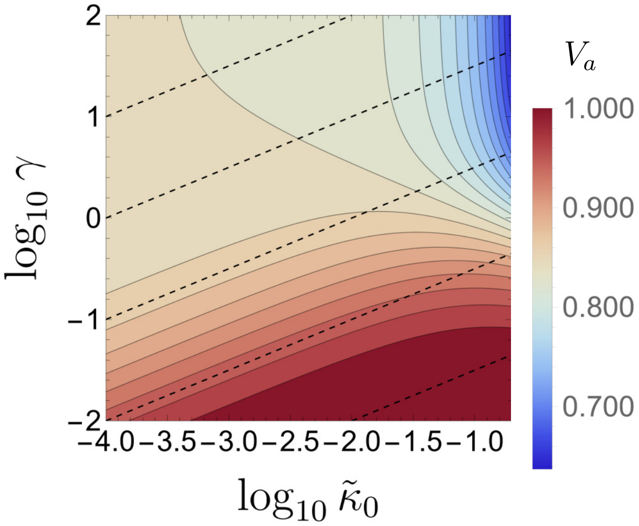

FIG. 8. Contour plots varying $\tilde{\kappa}_0$ and γ of the particle velocity when the particle is positioned along the center line of the tube ($\beta = 0$) with $\alpha = 2$. The dashed lines are lines of fixed $\tilde{\gamma}$ and vary from 10^{-1} to 10^{3} in powers of 10.

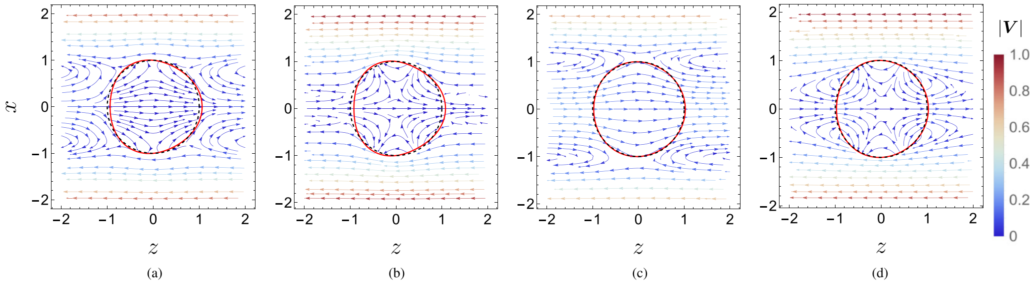

FIG. 9. Streamline plots under an external Poiseuille flow varying $\tilde{\kappa}_0$ and γ; $\beta = 0$ and $\alpha = 2$ in all plots. The undeformed and deformed ($\epsilon = 0.4$, $\nu = 0.25$) particle surfaces are presented via the black dashed and red lines, respectively. In (a) $(\tilde{\kappa}_0, \gamma) = (0.001, 100)$, (b) $(0.001, 0.01)$, (c) $(0.1, 100)$, and (d) $(0.1, 0.01)$. From left to right the particle velocities are 0.83, 0.99, 0.74, 0.99.

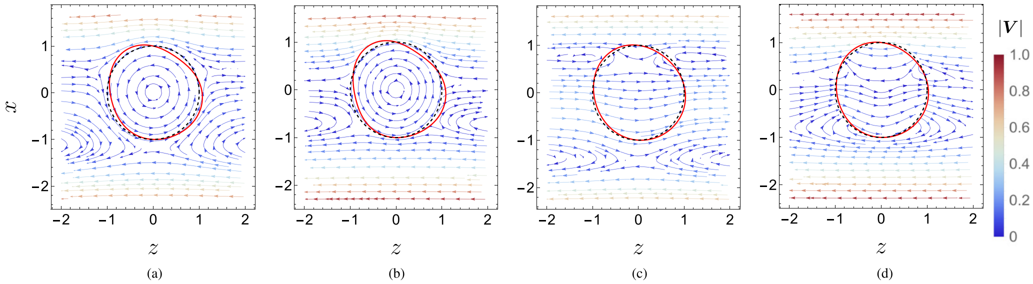

FIG. 10. Streamline plots under an external Poiseuille flow varying $\tilde{\kappa}_0$ and γ; $\beta = 1/3$ and $\alpha = 2$ in all plots. The undeformed and deformed ($\epsilon = 0.4$, $\nu = 0.25$) particle surfaces are presented via the black dashed and red lines, respectively. In (a) $(\tilde{\kappa}_0, \gamma) = (0.001, 100)$, (b) $(0.001, 0.01)$, (c) $(0.1, 100)$, and (d) $(0.1, 0.01)$. From left to right the particle velocities are 0.80, 0.95, 0.71, 0.97.

The dimensionless background Poiseuille flow may be written as

$$\boldsymbol{V}^e = [a + bx + c(x^2 + y^2)]\boldsymbol{e}_z, \tag{4.11}$$

$$a = \left(1 - \frac{\beta^2}{\alpha^2}\right) - V_a, \quad b = -\frac{2\beta}{\alpha^2}, \quad c = -\frac{1}{\alpha^2}. \tag{4.12}$$

The background Poiseuille flow is written exactly using the solid spherical harmonics by setting

$$\Phi_1* = az, \quad \Phi_2* = \frac{b}{2}xz, \quad \Phi_3* = -\frac{c}{15}(5z^3 - 3r^2 z), \quad P_1* = 4cz, \quad \Psi_1* = -\frac{b}{2}y. \tag{4.13}$$

Using Eq. (3.21) we obtain the translational and angular velocity of the particle. In particular, the translation velocity is given by

$$V_a = 1 - \alpha^{-2}\left(\beta^2 + \frac{2}{3}Q(\tilde{\kappa}_0, \tilde{\gamma})\right), \quad Q(\tilde{\kappa}_0, \tilde{\gamma}) = \frac{\tilde{\gamma}(1 + 6\tilde{\kappa}_0)}{2 + \tilde{\gamma} + 4\tilde{\kappa}_0\tilde{\gamma}}, \tag{4.14}$$

and the angular velocity is

$$\Omega^x = \Omega^z = 0, \quad \Omega^y = -\frac{b}{2} = \frac{\beta}{\alpha^2}. \tag{4.15}$$

Here the particle rotation is caused by the particle being off-axis which is captured through the bx shearing term in Eq. (4.11). The surface deformation of the particle is then given by

$$r_s = 1 - \epsilon\alpha^{-2}\left(\frac{5}{2}\beta L^s(\tilde{\kappa}_0, \tilde{\gamma}, \nu)\sin 2\theta\cos\phi - \frac{7}{16}L^p(\tilde{\kappa}_0, \tilde{\gamma}, \nu)(5\cos^3\theta - 3\cos\theta)\right), \tag{4.16}$$

where $L^s(\tilde{\kappa}_0, \tilde{\gamma}, \nu)$ is given in Eq. (4.6) and is due to the shearing component of the background Poiseuille flow and is proportional to β, and $L^p(\tilde{\kappa}_0, \tilde{\gamma}, \nu) \in [0, 1]$ is given by

$$L^p(\tilde{\kappa}_0, \tilde{\gamma}, \nu) = \frac{4[30(3 + \nu) + \tilde{\gamma}(5 + 23\nu)]}{[28 + 570\tilde{\kappa}_0 + \tilde{\gamma}(4 + 57\tilde{\kappa}_0)](13 + 7\nu)}. \tag{4.17}$$

Again taking the limits $\nu \to 1/2, \tilde{\gamma} \to \infty$ and $\tilde{\kappa}_0 \to 0$ we observe that $Q(\tilde{\kappa}_0, \tilde{\gamma}) \to 1$, $L^s(\tilde{\kappa}_0, \tilde{\gamma}, \nu) \to 1$ and $L^p(\tilde{\kappa}_0, \tilde{\gamma}, \nu) \to 1$ to again exactly recover the translational and rotational velocities, and the surface deformation obtained by Murata [30] for an incompressible, no-slip, impermeable elastic particle. As with the case of shear flow, the rigid body rotation does not depend on the choice of $\tilde{\kappa}_0$ and $\tilde{\gamma}$.

For completeness, we additionally write the Darcy pressure and shearing surface tractions

$$p_f = \frac{5\beta}{2\alpha^2}M^s(\tilde{\kappa}_0, \tilde{\gamma})r^2\sin 2\theta\cos\phi + M^p(\tilde{\kappa}_0, \tilde{\gamma})r^3(5\cos^3\theta - 3\cos\theta) - \frac{r}{\alpha^2}\frac{4\tilde{\gamma}\cos\theta}{2 + \tilde{\gamma}}, \tag{4.18}$$

$$\boldsymbol{\tau}\cdot\boldsymbol{e}_\theta = -\frac{5\beta}{2\alpha^2}T^s(\tilde{\kappa}_0, \tilde{\gamma})r^2\cos 2\theta\cos\phi + T^p(\tilde{\kappa}_0, \tilde{\gamma})r^3\sin\theta(5\cos^2\theta - \cos\theta) + \frac{1}{\alpha^2}\frac{2\tilde{\gamma}\sin\theta}{2 + \tilde{\gamma}}, \tag{4.19}$$

$$\boldsymbol{\tau}\cdot\boldsymbol{e}_\phi = \frac{5\beta}{2\alpha^2}T^s(\tilde{\kappa}_0, \tilde{\gamma}), \tag{4.20}$$

where $M^s(\tilde{\kappa}_0, \tilde{\gamma})$ and $T^s(\tilde{\kappa}_0, \tilde{\gamma})$ given in Eqs. (4.7) and (4.8) and the functions $M^p(\tilde{\kappa}_0, \tilde{\gamma})$ and $T^p(\tilde{\kappa}_0, \tilde{\gamma})$ are given by

$$M^p(\tilde{\kappa}_0, \tilde{\gamma}) = \left(\frac{10}{\tilde{\gamma}} + 1\right)T^p(\tilde{\kappa}_0, \tilde{\gamma}), \quad T^p(\tilde{\kappa}_0, \tilde{\gamma}) = \frac{4\tilde{\gamma}}{4(7 + \tilde{\gamma}) + 57\tilde{\kappa}_0(10 + \tilde{\gamma})}. \tag{4.21}$$

We note that T^p does not feature in τ_ϕ since the background Poiseuille flow is axisymmetric when $\beta = 0$. It may be shown that the final terms in Eqs. (4.18) and (4.19) generate a deformation which does not represent a departure from a sphere; specifically, they correspond to a translation of the coated cell along the z axis. We note that this translation is omitted in Eq. (4.16).

In Fig. 8 we present contour plots of the translational velocity of the particle positioned along the center line of the tube ($\beta = 0$) with $\alpha = 2$. In general the velocity decreases as we increase γ, since the decreased slip increases the particle drag. When γ is large, an increase in Darcy number decreases the translational velocity, since the fluid flows through the particle rather than driving it downstream. However, when γ is small, increasing the Darcy number increases the particle velocity due to the effective reduction in slip via Eq. (2.25). The effect of the Darcy number is smaller when γ is small since the greater slip leads to the fluid preferentially flowing around the particle rather than through it. In the limiting case of perfect slip ($\gamma = 0$), we have the maximal particle velocity $V_a = 1$. If instead we consider the dashed lines of fixed $\tilde{\gamma}$ in Fig. 8, the impact of the Darcy number through Eq. (2.25) is removed, and we observe that the particle velocity always decreases with $\tilde{\kappa}_0$. When the particle is off-axis ($\beta \neq 0$), the particle velocity V_a contains the additive constant $-\beta^2/\alpha^2$ which is independent of γ and $\tilde{\kappa}_0$. Increasing β has the effect of decreasing the average velocity of the surrounding flow, while inducing the rotation captured in Eq. (4.15).

We present 2D cross sections (z-x plane) of the streamlines and equilibrium particle shape under Poiseuille flow in Fig. 9, fixing $\beta = 0$ such that the particle is in the center of the tube, and varying $\tilde{\kappa}_0$ and γ. In the external region we plot the velocity field $\boldsymbol{V}$, and inside the particle we plot the total volumetric flux $\boldsymbol{q}$, and the streamline color reflects the velocity magnitude. We set $\alpha = 2$ throughout and choose $\epsilon = 0.4$ such that the surface deformation is comparable to those presented in Fig. 4. We note that since the particle translates in the laboratory frame, with its translational velocity $\boldsymbol{V}_{tr} = V_a \boldsymbol{e}_z$ given by Eq. (4.14), the tube wall velocity differs slightly in each plot, as detailed in the figure caption. In all plots, flow close to the tube wall moves to the left (upstream) due to the sliding wall, and flow close to the center-line moves to the right (downstream) due to the Poiseuille flow.

Figures 9(a) and 9(b) have small Darcy number such that the internal flow is small. When γ is large in Fig. 9(a) the external streamlines bend such that the upstream flow close to the tube wall and downstream flow close to the tube axis are connected. In Fig. 9(b) when γ is small, these bends are sharper since the increased slip allows an increased flow around the particle. The increased slip causes the particle velocity to increase, changing the internal flow pattern such that we observe upstream flow within the particle. In Fig. 9(c) we again have a small slip $\gamma = 100$ and increase the Darcy number. This increase in the Darcy number reduces the downstream force imposed on the particle by the external fluid, calculated via the stress integral (2.6), decreasing the particle velocity. Further, the external streamlines are more horizontal, since less fluid is diverted around the particle surface. Increasing the slip ($\gamma = 0.01$) in Fig. 9(d) the particle mobility is again increased, and we observe a similar internal flow profile to that in Fig. 9(b), since fluid may more easily slip around the particle rather than travel through it. Compared with Fig. 9(b), the increase in Darcy number results in recirculation regions which cross the particle surface. We note that these recirculation regions are a result of the reference frame and are not present in the laboratory frame.

In Fig. 10 we present 2D streamline plots for an off-axis poroelastic particle in Poiseuille flow, fixing $\beta = 1/3$ and varying $\tilde{\kappa}_0$ and γ. Compared with Fig. 9 the particle velocity is decreased by β^2/α^2 and the particle rotates according to Eq. (4.15). With a small Darcy number in Figs. 10(a) and 10(b), the internal streamlines are circular due to this rotation. However, increasing the Darcy number in Figs. 10(c) and 10(d), the fluid instead transits through the particle. In both Figs. 9 and 10, we note that the tube wall boundary conditions are not strongly disrupted, especially when the Darcy number is larger. In fact, only the topmost streamlines in Figs. 10(a) and 10(b) are visibly perturbed from horizontal.

When on the center line ($\beta = 0$), the particle adopts a bullet-like shape, which is consistent with previous observations for an elastic particle [30,33,34]. When off-axis, the particle shape is a linear combination of a bullet-like deformation associated with the Poiseuille flow and the prolate spheroid deformation associated with a shear flow of strength b. From Eq. (4.16), we note that the surface deformation is proportional to α^{-2}. This is expected since in the limiting case of $\alpha \to \infty$

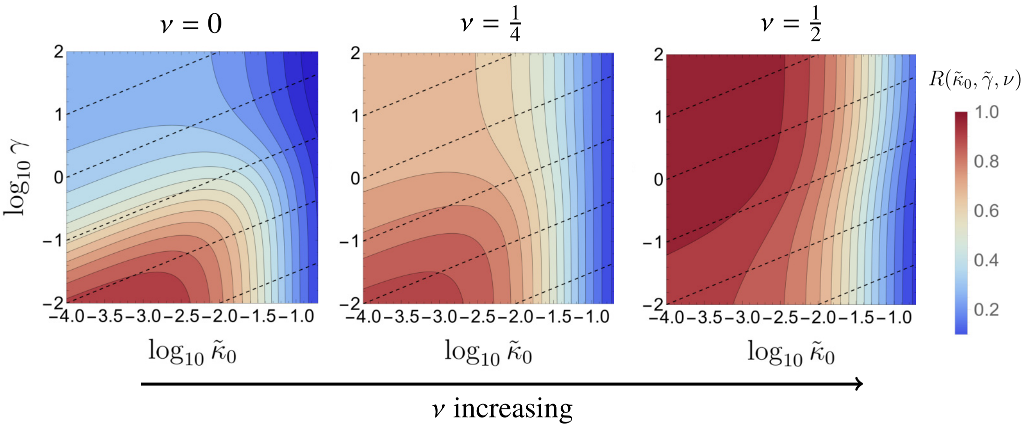

FIG. 11. Contour plots of the magnitude of the particle surface deformation when $\beta = 0$, $L^p(\tilde{\kappa}_0, \tilde{\gamma}, \nu)$. We continuously vary $\tilde{\kappa}_0$ and γ and use the discrete values of $\nu = 0, 1/4, 1/2$. The dashed lines are lines of fixed $\tilde{\gamma}$, and vary from 10^{-1} to 10^{3} in powers of 10.

the background flow is uniform, which generates no surface deformation for a nonporous elastic particle [31].

Having previously presented contour plots of $L^s(\tilde{\kappa}_0, \tilde{\gamma}, \nu)$ in Fig. 6, we now present contour plots of the surface deformation magnitude for a particle on the center line of the tube ($\beta = 0$) in Fig. 11, given by $L^p(\tilde{\kappa}_0, \tilde{\gamma}, \nu)$ (4.16). The Darcy number $\tilde{\kappa}_0$ and slip parameter γ are varied continuously for the discrete values of Poisson's ratio, $\nu = 0, 1/4, 1/2$. We observe similar dependencies on $\tilde{\kappa}_0$, γ, and ν, which we again attribute to the effects of the Darcy pressure and normal/shearing fluid tractions. With large γ the sliding wall generates a larger shearing traction on the particle surface. As before, with $\nu = 1/2$ transverse strains are developed within the particle such that an increase in γ increases the surface deformation magnitude. With $\nu = 0$, no such transverse strains are developed such that we observe the reverse dependency. Similar to Eq. (4.9), we write the surface deformation (4.16) as a combination of the Darcy pressure (4.21) and shearing traction (4.21) magnitudes,

$$L^p(\tilde{\kappa}_0, \tilde{\gamma}, \nu) = \frac{3(3+\nu)}{(13+7\nu)} M^p(\tilde{\kappa}_0, \tilde{\gamma}) + \frac{4(5\nu-1)}{(13+7\nu)} T^p(\tilde{\kappa}_0, \tilde{\gamma}). \tag{4.22}$$

Similar to Eq. (4.9), we see that as ν increases, the contribution from the Darcy pressure decreases, and the contribution from the shearing traction increases. However, unlike in Eq. (4.9), here the shearing traction generates a surface deformation when $\nu = 0$. We attribute this to the more complex θ dependence (larger n in the solid spherical harmonic functions) of the shearing traction in Eq. (4.21). When $\nu = 1/5$, we see that the base contribution (when $\nu = 0$) of the shearing traction to the surface deformation exactly cancels the contribution due to the transverse strains developed within the particle.

V. DISCUSSION

We develop a framework to model an initially spherical poroelastic particle exposed to a general background Stokes flow. We assume the ratio of the viscous fluid stress to the elastic stiffness is small such that the particle is governed by the equations of linear poroelasticity. To demonstrate the power of the framework, we analytically investigate the impacts of the Darcy number, slip, and Poisson's ratio on the particle's translation, rotation, and deformation, presenting results under a background shear and Poiseuille flow. We acknowledge that in the latter case the external tube boundary is not explicitly accounted for. Nevertheless, the results in Sec. IV B are valid provided the particle is sufficiently far from the external boundary. The presented framework allows the theoretical consideration of external flows involving any external boundary, provided they can be treated as unbounded, that is, the background flow can be written as a finite sum of spherical harmonics.

For both a background shear and Poiseuille flow, our solutions agree exactly with those presented by Murata [30] in the limiting case of an nonporous, incompressible elastic particle with no-slip boundary conditions. Under a shear flow the particle rotates, with different flow patterns observed for varying slip. Interestingly, the leading-order particle rotation does not depend on its poroelasticity, since the torque imposed on the particle by the shear flow scales identically with the torque required to generate its rotation. We find that the surface displacement decreases with increasing Darcy number and, surprisingly, may either increase or decrease with increasing slip, depending on the Poisson's ratio. We interpret this latter dependency by considering the Darcy pressure and fluid tractions which drive the resulting deformation. Under a background Poiseuille flow the particle translates; its mobility is decreased with the Darcy number and enhanced by a large slip. When positioned on the tube center line the particle obtains a bullet-like shape, with similar dependencies to those observed for a shear flow. When off-axis, a shearing component is introduced in the background flow which causes the particle to translate more slowly, rotate, and deform according to the magnitude of the shear. In general, we predict the deformation magnitude depends on the square of the tube radius.

The framework developed above offers many potential applications and extensions. For example, the sedimentation dynamics of a compressible elastic particle in a confined geometry is not well understood [51] and may be modeled using our framework through the inclusion of a body force. Additionally, our framework may be used to benchmark numerical simulations with varying geometries and could also be used for the rapid determination of material properties via microfluidic systems, for example, in flow cytometry [35]. The framework can also be applied to spherical particles with a core-shell structure. The shell could represent a poroelastic coating that surrounds a fluid or solid core, which could be used as a model for hydrogel-coated therapeutic cells that are injected into the body [13]. More complex physics may also be incorporated into our framework. For example, the general solutions for both a Brinkman medium and a poro-viscoelastic medium are readily available using spherical harmonics (ignoring inertial terms), with the latter containing strong applications to cell modeling [18,52]. To implement these physics, the desired general solution may replace the general solution to Darcy's law (3.9) when solving the fluid problem. Recently, Xu *et al.* [43] investigated the impact of four different sets of boundary conditions coupling a Stokes flow to a poroelastic domain, concluding that a combination of complex flows and geometry are required to discriminate between them. Each of these different sets of interfacial conditions may be similarly reformulated and considered using our framework, which would allow analytical solutions to be produced that could greatly facilitate the validation of different boundary conditions.

ACKNOWLEDGMENTS

This work was supported by an Engineering and Physical Sciences Research Council studentship (EP/V520202/1) (S.M.F.). S.L.W. gratefully acknowledges funding from the MRC (MR/T015489/1).

The authors report no conflict of interest.

DATA AVAILABILITY

An implementation of the above framework in *Mathematica* may be found on GitHub [53].

APPENDIX A: COORDINATE TRANSFORMATIONS

We present transformations between the spherical and Cartesian coordinate systems used in this work. For both coordinate systems it is convenient to define the origin as the center of the undeformed particle. Following convention, we align the "north pole" of the sphere with the positive

z axis, to obtain the following relations:

$$\begin{pmatrix} \sin\theta\cos\phi & \cos\theta\cos\phi & -\sin\phi \\ \sin\theta\sin\phi & \cos\theta\sin\phi & \cos\phi \\ \cos\theta & -\sin\theta & 0 \end{pmatrix}\begin{pmatrix} \boldsymbol{e}_r \\ \boldsymbol{e}_\theta \\ \boldsymbol{e}_\phi \end{pmatrix} = \mathcal{A}\begin{pmatrix} \boldsymbol{e}_r \\ \boldsymbol{e}_\theta \\ \boldsymbol{e}_\phi \end{pmatrix} = \begin{pmatrix} \boldsymbol{e}_x \\ \boldsymbol{e}_y \\ \boldsymbol{e}_z \end{pmatrix}, \quad \text{with} \quad \begin{matrix} x = r\sin\theta\cos\phi \\ y = r\sin\theta\sin\phi, \\ z = r\cos\theta \end{matrix} \tag{A1}$$

where $\mathcal{A}$ is orthogonal. To transform a vector, $\boldsymbol{V}$, and a tensor, $\boldsymbol{\sigma}$, between these coordinate systems we write

$$\boldsymbol{V}(r, \theta, \phi) = \mathcal{A}\boldsymbol{V}(x, y, z), \tag{A2}$$

$$\boldsymbol{\Sigma}(r, \theta, \phi) = \mathcal{A}\boldsymbol{\Sigma}(x, y, z)\mathcal{A}^T. \tag{A3}$$

APPENDIX B: SOLID SPHERICAL HARMONICS

We assume the function $h(\boldsymbol{r})$ satisfies Laplace's equation such that

$$\nabla^2 h = 0. \tag{B1}$$

Using a spherical coordinate system we have separable solutions,

$$h(\boldsymbol{r}) = \sum_{n=0}^{\infty}\sum_{m=-n}^{n}\left[h^{\mathcal{R}}_{n,m}\mathcal{R}_{n,m}(\boldsymbol{r}) + h^{\mathcal{I}}_{n,m}\mathcal{I}_{n,m}(\boldsymbol{r})\right], \tag{B2}$$

where $h^{\mathcal{R}}_{n,m}$ and $h^{\mathcal{I}}_{n,m}$ are constants, and $\mathcal{R}_{n,m}(\boldsymbol{r})$ and $\mathcal{I}_{n,m}(\boldsymbol{r})$ are the regular and irregular solid spherical harmonics, given by

$$\mathcal{R}_{n,m}(\boldsymbol{r}) = \sqrt{\frac{4\pi}{2n+1}}r^n Y_{n,m}(\theta, \phi), \quad \text{and} \quad \mathcal{I}_{n,m}(\boldsymbol{r}) = \sqrt{\frac{4\pi}{2n+1}}\frac{Y_{n,m}(\theta, \phi)}{r^{n+1}}. \tag{B3}$$

Here $Y_{n,m}(\theta, \phi)$ are Laplace's spherical harmonics. Restricting to the purely real case,

$$Y_{n,m}(\theta, \phi) = \begin{cases} (-1)^m\sqrt{\frac{(2n+1)}{2\pi}\frac{(n-|m|)!}{(n+|m|)!}}\mathcal{P}_{n,|m|}(\cos\theta)\sin|m|\phi, & m < 0 \\ \sqrt{\frac{(2n+1)}{4\pi}}P_{n,m}(\cos\theta), & m = 0 \\ (-1)^m\sqrt{\frac{(2n+1)}{2\pi}\frac{(n-m)!}{(n+m)!}}\mathcal{P}_{n,m}(\cos\theta)\sin m\phi, & m > 0, \end{cases} \tag{B4}$$

where $\mathcal{P}_{n,m}(\cos\theta)$ are the associated Legendre polynomials of degree n and order m. Written in this form we have the orthogonality relations,

$$\int_{\phi=0}^{2\pi}\int_{\theta=0}^{\pi} Y_{n,m}(\theta, \phi)Y_{p,q}(\theta, \phi)\sin\theta \, \mathrm{d}\theta \, \mathrm{d}\phi = \delta_{np}\delta_{mq}. \tag{B5}$$

Throughout much of the above work, for example in Sec. III A, it is convenient to consider only solid spherical harmonic functions of degree n. For clarity we write

$$h_n(\boldsymbol{r}) = \sum_{m=-n}^{n} h^{\mathcal{R}}_{n,m}\mathcal{R}_{n,m}(\boldsymbol{r}), \quad h_{-n-1}(\boldsymbol{r}) = \sum_{m=-n}^{n} h^{\mathcal{I}}_{n,m}\mathcal{I}_{n,m}(\boldsymbol{r}), \tag{B6}$$

where again $h^{\mathcal{R}}_{n,m}$ and $h^{\mathcal{I}}_{n,m}$ are constant coefficients. Note

$$h(\boldsymbol{r}) = \sum_{n=-\infty}^{\infty} h_n(\boldsymbol{r}), \tag{B7}$$

from Eq. (B2).

Useful identities

We now present several identities involving the solid spherical harmonics which will be useful when reformulating the boundary conditions. Assuming h_n is a solid spherical harmonic function of degree n,

$$x\frac{\partial h_n}{\partial x}+y\frac{\partial h_n}{\partial y}+z\frac{\partial h_n}{\partial z}=r\frac{\partial h_n}{\partial r}=nh_n, \tag{B8}$$

$$\nabla^2(r^l h_n)=l(l+2n+1)r^{l-2}h_n. \tag{B9}$$

We also quote the vector calculus identity with $\boldsymbol{A}$ an arbitrary vector,

$$\nabla\times(\nabla\times\boldsymbol{A})=\nabla(\nabla\cdot\boldsymbol{A})-\nabla^2\boldsymbol{A}. \tag{B10}$$

APPENDIX C: THE REDUCTION TO AN IMPERMEABLE, INCOMPRESSIBLE PARTICLE SUBJECT TO NO-SLIP BOUNDARY CONDITIONS

Through the interfacial conditions (2.22) and (2.23) we have

$$\Sigma_{rr}=-p_f, \tag{C1}$$

$$\Sigma_{rr}=-p_f+\frac{2\nu}{1-2\nu}\nabla\cdot\boldsymbol{u}+2\frac{\partial u_r}{\partial r}, \tag{C2}$$

which combined also require Eq. (2.26),

$$2\frac{\partial u_r}{\partial r}=-\frac{2\nu}{1-2\nu}\nabla\cdot\boldsymbol{u}, \tag{C3}$$

on $r=1$.

We now consider the limiting case of $\nu\to 1/2$. Defining the small parameter $\delta=(1-2\nu)\ll 1$, it may be shown that as $\delta\to 0$

$$\nabla\cdot\boldsymbol{u}=O(\delta)+\cdots. \tag{C4}$$

We then write the Darcy pressure as

$$p_f=p_{\text{elas}}+\frac{2\nu}{1-2\nu}\nabla\cdot\boldsymbol{u}, \tag{C5}$$

where p_{elas} is the solid elastic pressure for the case of an impermeable, incompressible particle subject to no-slip boundary conditions, as obtained by Murata [30]. Since the particle is incompressible, p_{elas} acts as a Lagrange multiplier to enforce Eq. (C4) when $\delta\to 0$. Using the pressure decomposition (C5), along with Eq. (C3), both interfacial conditions (C1) and (C2) become

$$\Sigma_{rr}=-p_{\text{elas}}+2\frac{\partial u_r}{\partial r}, \tag{C6}$$

such that we recover the expected stress balance between the Stokes flow and elastic particle. Using Eq. (C5), it can be shown that our predictions for the solid elastic pressure are in perfect agreement with those presented by Murata [30].

---

[1] D. Caccavo, An overview on the mathematical modeling of hydrogels' behavior for drug delivery systems, Int. J. Pharm. **560**, 175 (2019).

[2] M. Penn and M. Hennessy, Optimal loading of hydrogel-based drug-delivery systems, Appl. Math. Modell. **112**, 649 (2022).

[3] J. Li and D. J. Mooney, Designing hydrogels for controlled drug delivery, Nat. Rev. Mater. **1**, 16071 (2016).

[4] M. Villone and P. Maffettone, Dynamics, rheology, and applications of elastic deformable particle suspensions: A review, Rheol. Acta **58**, 109 (2019).

[5] M. M. Villone, J. K. Nunes, Y. Li, H. A. Stone, and P. L. Maffettone, Design of a microfluidic device for the measurement of the elastic modulus of deformable particles, Soft Matter **15**, 880 (2019).

[6] Y. Chen, K. Guo, L. Jiang, S. Zhu, Z. Ni, and N. Xiang, Microfluidic deformability cytometry: A review, Talanta **251**, 123815 (2023).

[7] A. K. Haudenschild, A. H. Hsieh, S. Kapila, and J. C. Lotz, Pressure and distortion regulate human mesenchymal stem cell gene expression, Ann. Biomed. Eng. **37**, 492 (2009).

[8] H. Zhang, A. Kay, N. R. Forsyth, K. K. Liu, and A. J. El Haj, Gene expression of single human mesenchymal stem cell in response to fluid shear, J. Tissue Eng. **3**, 2041731412451988 (2012).

[9] H. Li, A. Muhammad, and P. Norbert, Mechanosensitive channels and their functions in stem cell differentiation, Exp. Cell Res. **374**, 259 (2019).

[10] B. Martinac, Y. A. Nikolaev, G. Silvani, N. Bavi, V. Romanov, Y. Nakayama, A. D. Martinac, P. Rohde, O. Bavi, and C. D. Cox, Cell membrane mechanics and mechanosensory transduction, Curr. Top. Membr. **86**, 83 (2020).

[11] F. M. Eroshkin and A. G. Zaraisky, Mechano-sensitive regulation of gene expression during the embryonic development, Genesis **55**, e23026 (2017).

[12] M. C. Arno, Engineering the mammalian cell surface with synthetic polymers: Strategies and applications, Macromol. Rapid Commun. **41**, 2000302 (2020).

[13] T. T. Pham, P. L. Tran, C. D. Phung, H. T. Nguyen, C. H. Nguyen, C. S. Yong, J. O. Kim, S. Yook, and J.-H. Jeong, Surface-triggered *in situ* gelation for tunable conformal hydrogel coating of therapeutic cells and biomedical devices, Adv. Funct. Mater. **31**, 2010169 (2021).

[14] M. Biot, General theory of three dimensional consolidation, J. Appl. Phys. **12**, 155 (1941).

[15] M. Biot, Nonlinear and semilinear rheology of porous solids, J. Geophys. Res. **78**, 4924 (1973).

[16] S. Whitaker, Flow in porous media I: A theoretical derivation of Darcy's law, Transp. Porous Media **1**, 3 (1986).

[17] L. Durlofsky and J. Brady, Analysis of the Brinkman equation as a model for flow in porous media, Phys. Fluids **30**, 3329 (1987).

[18] B. Padmavathi, T. Amaranath, and S. Nigam, Stokes flow past a porous sphere using Brinkman's model, Z. Angew. Math. Phys. **44**, 929 (1993).

[19] S.-M. Yang and W.-H. Hong, Motions of a porous particle in Stokes flow: Part 1. Unbounded single-fluid domain problem, Korean J. Chem. Eng. **5**, 23 (1988).

[20] S.-M. Yang and W.-H. Hong, Motions of a porous particle in Stokes flow part 2. Linear flows near a fluid interface, Korean J. Chem. Eng. **6**, 234 (1989).

[21] S.-M. Yang and L. G. Leal, Motions of a porous particle in Stokes-flow near a plane-fluid interface, Physicochemical Hydrodynamics **11**, 543 (1989).

[22] E. Saad and M. Faltas, Slow motion of a porous sphere translating along the axis of a circular cylindrical pore subject to a stress jump condition, Transp. Porous Media **102**, 91 (2014).

[23] J. Prakash and G. Sekhar, Slow motion of a porous spherical particle with a rigid core in a spherical fluid cavity, Meccanica **52**, 91 (2017).

[24] X. Yao, C. Ng, J. Teo, Marcos, and T. Wong, Slow viscous flow of two porous spherical particles translating along the axis of a cylinder, J. Fluid Mech. **861**, 643 (2019).

[25] C. Peskin, The immersed boundary method, Acta Numerica **11**, 479 (2002).

[26] W. Strychalski, C. Copos, O. Lewis, and R. Guy, A poroelastic immersed boundary method with applications to cell biology, J. Comput. Phys. **282**, 77 (2015).

[27] C. Copos and R. Guy, A porous viscoelastic model for the cell cytoskeleton, ANZIAM J. **59**, 472 (2018).

[28] Y. Leng, M. de Lucio, and H. Gomez, Using poro-elasticity to model the large deformation of tissue during subcutaneous injection, Comput. Methods Appl. Mech. Eng. **384**, 113919 (2021).

[29] L. Li, J. Zhang, Z. Xu, Y.-N. Young, J. Feng, and P. Yue, An arbitrary Lagrangian-Eulerian method for simulating interfacial dynamics between a hydrogel and a fluid, J. Comput. Phys. **451**, 110851 (2022).

[30] T. Murata, Deformation of an elastic particle suspended in an arbitrary flow field, J. Phys. Soc. Jpn. **50**, 1009 (1981).

[31] B. Nasouri, A. Khot, and G. Elfring, Elastic two-sphere swimmer in Stokes flow, Phys. Rev. Fluids **2**, 043101 (2017).

[32] Y.-N. Young, Y. Mori, and M. J. Miksis, Slightly deformable Darcy drop in linear flows, Phys. Rev. Fluids **4**, 063601 (2019).

[33] M. M. Villone, F. Greco, M. A. Hulsen, and P. L. Maffettone, Numerical simulations of deformable particle lateral migration in tube flow of Newtonian and viscoelastic media, J. Non-Newtonian Fluid Mech. **234**, 105 (2016).

[34] S. M. Finney, M. G. Hennessy, A. Münch, and S. L. Waters, The impact of confinement on the deformation of an elastic particle under axisymmetric tube flow, IMA J. Appl. Math. **89**, 498 (2024).

[35] A. Mietke, O. Otto, S. Girardo, P. Rosendahl, A. Taubenberger, S. Golfier, E. Ulbricht, S. Aland, J. Guck, and E. Fischer-Friedrich, Extracting cell stiffness from real-time deformability cytometry: Theory and experiment, Biophys. J. **109**, 2023 (2015).

[36] H. Brenner and J. Happel, Slow viscous flow past a sphere in a cylindrical tube, J. Fluid Mech. **4**, 195 (1958).

[37] G. S. Beavers and D. Joseph, Boundary conditions at a naturally permeable wall, J. Fluid Mech. **30**, 197 (1967).

[38] P. Saffman, On the boundary condition at the surface of a porous medium, Stud. Appl. Math. **50**, 93 (1971).

[39] T. Levy and E. Sanchez-Palencia, On boundary conditions for fluid flow in porous media, Int. J. Eng. Sci. **13**, 923 (1975).

[40] J. Ochoa-Tapia and S. Whitaker, Momentum transfer at the boundary between a porous medium and a homogeneous fluid—I. Theoretical development, Int. J. Heat Mass Transf. **38**, 2635 (1995).

[41] M. Minale, Momentum transfer within a porous medium. II. Stress boundary condition, Phys. Fluids **26**, 123102 (2014).

[42] J. J. Feng and Y.-N. Young, Boundary conditions at a gel-fluid interface, Phys. Rev. Fluids **5**, 124304 (2020).

[43] Z. Xu, J. Zhang, Y.-N. Young, P. Yue, and J. Feng, Comparison of four boundary conditions for the fluid-hydrogel interface, Phys. Rev. Fluids **7**, 093301 (2022).

[44] R. Ruiz-Baier, M. Taffetani, H. D. Westermeyer, and I. Yotov, The Biot–Stokes coupling using total pressure: Formulation, analysis and application to interfacial flow in the eye, Comput. Methods Appl. Mech. Eng. **389**, 114384 (2022).

[45] S. Badia, A. Quaini, and A. Quarteroni, Coupling Biot and Navier–Stokes equations for modeling fluid–poroelastic media interaction, J. Comput. Phys. **228**, 7986 (2009).

[46] C. W. MacMinn, E. R. Dufresne, and J. S. Wettlaufer, Large deformations of a soft porous material, Phys. Rev. Appl. **5**, 044020 (2016).

[47] See Supplemental Material at http://link.aps.org/supplemental/10.1103/p3g6-gkww for the asymptotic reduction of the nonlinear problem, as well as the reformulation of the interfacial conditions for the fluid and solid problems, which includes Refs. [30,37,46,54,55].

[48] H. Lamb, *Hydrodynamics*, 6th ed. (Dover, New York, 1945), pp. 595–596.

[49] P. Howell, G. Kozyreff, and J. Ockendon, *Applied Solid Mechanics*, Cambridge Texts in Applied Mathematics (Cambridge University Press, Cambridge, 2008).

[50] T. Tran-Cong, On the completeness of the Papkovich-Neuber solution, Q. Appl. Math. **47**, 645 (1989).

[51] I. Noichl and C. Schönecker, Dynamics of elastic, nonheavy spheres sedimenting in a rectangular duct, Soft Matter **18**, 2462 (2022).

[52] M. Moradi, W. Shi, and E. Nazockdast, General solutions of linear poro-viscoelastic materials in spherical coordinates, J. Fluid Mech. **946**, A22 (2022).

[53] S. M. Finney, Poroelastic sphere unbounded, GitHub repository (2024), https://github.com/finneysimon/PoroelasticSphereUnbounded.

[54] S. N. Atluri and A. Cazzani, Rotations in computational solid mechanics, Arch. Comput. Methods Eng. **2**, 49 (1995).

[55] J. Happel and H. Brenner, *Low Reynolds Number Hydrodynamics*, 1st ed., Mechanics of Fluids and Transport Processes (Springer Dordrecht, 1983).